Science of the Total Environment 852 (2022) 158459

Contents lists available at ScienceDirect

Science of the Total Environment

journal homepage: www.elsevier.com/locate/scitotenv

Emission, transport, deposition, chemical and radiative impacts of mineral dust during severe dust storm periods in March 2021 over East Asia

Lin Liang [a,b], Zhiwei Han [a,b,*], Jiawei Li [a], Xiangao Xia [c], Yele Sun [d,b], Hong Liao [e], Ruiting Liu [f], Mingjie Liang [a,b], Yuan Gao [g], Renjian Zhang [c]

[a] Key Laboratory of Regional Climate-Environment for Temperate East Asia, Institute of Atmospheric Physics, Chinese Academy of Sciences, Beijing 100029, China
[b] University of Chinese Academy of Sciences, Beijing 100049, China
[c] Key Laboratory of Middle Atmosphere and Global Environment Observation, Institute of Atmospheric Physics, Chinese Academy of Sciences, Beijing 100029, China
[d] State Key Laboratory of Atmospheric Boundary Layer Physics and Atmospheric Chemistry, Institute of Atmospheric Physics, Chinese Academy of Sciences, Beijing 100029, China
[e] Jiangsu Key Laboratory of Atmospheric Environment Monitoring and Pollution Control, Jiangsu Collaborative Innovation Center of Atmospheric Environment and Equipment Technology, School of Environmental Science and Engineering, Nanjing University of Information Science and Technology, Nanjing 210044, China
[f] Institute of Urban Meteorology, China Meteorological Administration, Beijing 100089, China
[g] Zhongwei Municipal Ecology and Environment Bureau, Zhongwei 755000, China

HIGHLIGHTS

- Severe dust storms over East Asia in March 2021 were explored with an improved dust model.
- Dust reduced surface solar radiation by 313 Wm^{-2} (72 %) when dust storm arrived in Beijing.
- Heterogeneous reaction was enhanced in dust backflow with moderate wind and increased RH.
- Wet deposition was two times the dry deposition in mainland China downwind of Gobi deserts.

GRAPHICAL ABSTRACT

(a) The FengYun-4A satellite image of the dust storm at 09:00 LST on 15 March 2021. The model simulated (b) change in daytime surface shortwave radiation due to dust extinction (W m − 2), (c) change in total nitrate concentration (μg m − 3) due to heterogeneous reactions on dust surface, (d) dust emission amount (Gg gird − 1), (d) dry deposition amount (Gg gird − 1), (f) wet deposition amount (Gg gird − 1) during the first dust storm on 14–17 March 2021.

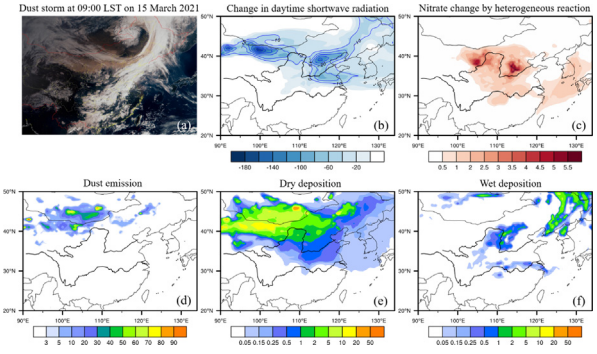

ARTICLE INFO

Editor: Anastasia Paschalidou

Keywords:
Mineral dust
Dust emission
Shortwave radiation
Photolysis rate
Heterogeneous reactions
Dry and wet depositions

ABSTRACT

A Regional Air Quality Model System (named RAQMS) coupled with a developed dust model driven by WRF was applied to synthetically investigate the emission, transport, deposition, budget, and chemical and radiative effects of mineral dust during the severe dust storm periods of 10–31 March 2021. Model results were validated against a variety of ground, vertical and satellite observations, which demonstrated a generally good model ability in reproducing meteorological variables, particulate matter and compositions, and aerosol optical properties. The first dust storm (DS1), which was the severest one since 2010 was originated from the Gobi Desert in southern Mongolia on 14 March, with the dust emission flux reaching 2785 μg m^{-2} s^{-1} and the maximum dust concentration exceeding 18,000 μg m^{-3} in the dust deflation region. This dust storm resulted in remarkably high hourly PM_{10} observations up to 7506 μg m^{-3}, 1887 μg m^{-3}, and 2704 μg m^{-3} in Beijing, Tianjin, and Shijiazhuang on 15 March, respectively, and led to a maximum decrease in surface shortwave radiation up to 313.4 W m^{-2} (72 %) in Beijing. The second dust storm (DS2) broke out

* Corresponding author at: Key Laboratory of Regional Climate-Environment for Temperate East Asia (RCE-TEA), Institute of Atmospheric Physics (IAP), Chinese Academy of Sciences (CAS), Beijing 100029, China.
E-mail address: hzw@mail.iap.ac.cn (Z. Han).

http://dx.doi.org/10.1016/j.scitotenv.2022.158459
Received 5 July 2022; Received in revised form 29 August 2022; Accepted 29 August 2022
Available online 3 September 2022

in the deserts of eastern Mongolia, with lower dust emission than the first one. The extinction of shortwave radiation by dust aerosols led to a reduction in photolysis rate and consequently decreases in O_3 and secondary aerosol concentrations over the North China Plain (NCP), whereas total sulfate and nitrate concentrations consistently increased due to heterogeneous reactions on dust surfaces over the middle reaches of the Yellow River and the NCP region during DS1. Sulfate and nitrate formation through heterogeneous reactions were enhanced in the dust backflow on 16–17 March by approximately 18 % and 24 % on average in the NCP. Heterogeneous reactions and photolysis rate reduction by mineral dust jointly led to average changes in sulfate, nitrate, ammonium, and secondary organic aerosol (SOA) concentrations by 13.0 %, 13.5 %, −12.3 %, and −4.4 %, respectively, in the NCP region during DS1, larger than the changes in the Yangtze River Delta (YRD). The maximum dry deposition settled in the 7–11 μm size range in downwind land and ocean areas, while wet deposition peaked in the 4.7–7 μm size range in the entire domain. Wet deposition was approximately twice the dry deposition over mainland China except for dust source regions. During 10–31 March, the total dust emission, dry and wet depositions were estimated to be 31.4 Tg, 13.78 Tg and 4.75 Tg, respectively, with remaining 12.87 Tg of dust aerosols (41 % of the dust emission) suspending in the atmosphere or transporting to other continents and oceans.

1. Introduction

Dust storm is a disastrous natural phenomenon and has significant impacts on air quality, human health, biogeochemical cycle, radiation balance, as well as climate change (Seinfeld et al., 2004; Shao and Dong, 2006; Faridi et al., 2021). Dust aerosols can be an effective platform for heterogeneous reactions by uptake of gaseous species and perturb atmospheric chemical system (Jacob, 2000; Tang et al., 2017). They also affect radiation and climate directly by absorbing/scattering shortwave/longwave radiation, or indirectly by acting as ice nuclei (Kaufman et al., 2002; DeMott et al., 2010). North Africa, Central and East Asia, Midwest America, and Central Australia were major dust source regions in the world and were frequently plagued by dust storms (Ginoux et al., 2004). The Gobi Desert in Mongolia and Inner Mongolia of China is one of the largest global dust sources, from which dust storms may influence broad regions of East Asia, and even North America through long-range transport (Uno et al., 2001; Zhang et al., 2003; Zhao et al., 2008; Li et al., 2011; Zhang et al., 2018).

Numerical model simulation is one of the essential ways to explore the deflation, transport, deposition, chemical and climatic impacts of mineral dust (Marticorena and Bergametti, 1995; Shao, 2001; Ginoux et al., 2001; Han et al., 2004). Previous studies promoted our understanding of dust aerosol characteristics and improved dust simulations at regional and global scales. Li et al. (2011) numerically investigated a severe dust storm on 19–23 March 2010 and found that dust aerosols comprised 30 %–60 % of PM_{10} mass concentration in North China, and 20 %–40 % in South China and the western Pacific regions. Dong et al. (2016) improved the dust emission model in CMAQ (Community Multiscale Air Quality model) and simulated the same dust storm in March 2010. Their model results showed that the dust aerosols affecting East China were originated from the Gobi Desert, and dust aerosols affecting Gansu province were originated from the Taklamakan Desert. Tian et al. (2021a) developed the dust scheme in GEOS-Chem by updating key parameters for dust deflation, and simulated a dust storm from 27 March to 2 April 2015 in North China, showing the spatial and temporal variation of mineral dust was better captured by the revised scheme. Ma et al. (2019) compared multimodel simulations of a dust storm during 4–6 May 2015 in North China. They found there were large discrepancies between predicted and observed PM_{10} concentrations in each model and suggested that dust source maps should be carefully selected on a regional scale. Chen et al. (2019) found that almost all the 14 global and regional chemical transport models participating in the Model Inter-Comparison Study for Asia phase III project underestimated PM_{10} levels over East Asia and suggested that dust models needed to be further developed.

Some studies investigated the radiative effects of dust aerosols and perturbation to tropospheric chemistry. Han et al. (2012) estimated the shortwave and longwave radiative effects of dust aerosols at the surface to be $-90\ W\ m^{-2}$ and $+40\ W\ m^{-2}$ over the Gobi Desert of East Asia during an intense dust storm on 19–22 March 2010. Li et al. (2017) investigated the effects of a typical dust storm during 16–18, March 2014 on ozone photochemistry in Nanjing using WRF-Chem, and found that the decreases in ground photolysis rate and OH concentration, along with changes in meteorological variables induced by dust aerosols led to lower photochemical activity and a small decrease in O_3 mixing ratio. Pan et al. (2017) observed that nitrate concentration in coarse mode increased and the depolarization ratio of particles decreased with the mixing of anthropogenic and dust pollution, suggesting nitrate formation through heterogeneous reaction on dust particles. Tian et al. (2021b) simulated with GEOS-Chem a dust event from 27 March to 2 April 2015 over North China and found the contribution of dust heterogeneous reactions to sulfate formation could be 20–30 %.

In recent years, the frequency and intensity of dust storms from the Gobi Desert of southern Mongolia and western China have decreased. However, during 14–17 March 2021, most of North and East China suffered from a strong dust storm which was the severest one since 2010, causing significant adverse effects on transportation, air quality, and even the loss of human lives in Mongolia. So far, only a few studies were conducted, focusing on the sources, evolutionary characteristics, synoptic weather conditions, boundary layer conditions and air quality impact of this strong dust storm (Liu et al., 2021; Yin et al., 2022; Filonchyk, 2022; Liang et al., 2022; Zhang et al., 2022; Jin et al., 2022). Yin et al. (2022) identified that the top-ranking anomalies of sea ice shift in the Barents and Kara Sea and the sea surface temperatures in east Pacific and northwest Atlantic induced the tremendous climate anomalies in dust source area, which combined with synoptic disturbances jointly facilitated the strongest spring sandstorm over the recent decade. Liu et al. (2021) investigated the extreme dust storm using CMAQ, and found the monthly average contribution of dust to PM_{10} concentration reached 47.4 % and 36.5 % in the Middle Yellow River Basin and Beijing-Tianjin-Hebei region, respectively. Liang et al. (2022) demonstrated that dust particles across northern China were composed of highly mixed materials from the erodible surface and a substantial component of fine sediments was initially emitted from Mongolia. Filonchyk (2022) explored the evolution of this dust storm by using integrated observations from ground-based sensors and satellites and indicated the dust coverage reached approximately 450,000 km^2, and there was a dense layer of dust extending from the surface to a height of about 8 km. Jin et al. (2022) conducted inverse modeling to simulate dust storms in spring 2021 through optimizing dust simulation with assimilation of MODIS aerosol optical depth (AOD) and ground-based PM_{10} observations and estimated that 19.9×10^6 t and 37.5×10^6 t of particles were released in the Chinese and Mongolian Gobi, respectively. In summary, modeling studies on this dust storm are very limited and all the above studies focus on physical processes, i.e., sources, transport, air quality, synoptic and boundary layer conditions, while a comprehensive investigation and understanding of the environmental effects of this dust storm are required.

In this study, a dust model is developed to represent dust deflation and emission more realistically. Model results are validated against a variety of observational data sets including surface measurements of meteorological

variables and particulate matter and its chemical components, meteorological soundings, AOD from AERONET and MODIS retrievals, vertical profiles of extinction coefficient from CALIPSO retrievals, surface shortwave radiation flux, as well as soil liquid water content from both ground measurement and satellite retrievals. A regional air quality model coupled with the developed dust model driven by WRF is applied to explore the emission, transport, deposition, and budget of mineral dust and the impacts of dust aerosols on shortwave radiation, photochemistry, and heterogeneous chemistry during the severe dust storms in March 2021. To our knowledge, this is the first synthetical study on the severe dust storms in spring 2021, which would provide new insight into evolution characteristics and environmental impacts of mineral dust over East Asia and could be helpful in the understanding of global dust budget and effects.

2. Model and observation descriptions

2.1. WRF

The Weather Research and Forecasting Model version 4.0 (WRF V4.0) is applied to provide meteorological fields for RAQMS, with four-dimensional data assimilation (4DDA) to enhance meteorological prediction. The six-hourly Global Final Reanalysis data is derived from the National Centers for Environment Prediction (NCEP) with a spatial resolution of 1° × 1° and used as initial and boundary meteorological conditions. Fig. 1 shows the study domain and observational sites for meteorology and aerosols.

The physical schemes used in WRF V4.0 for this study are as follows: the WSM 6-class graupel microphysical scheme (Hong and Lim, 2006), RRTMG shortwave and longwave radiation scheme (Iacono et al., 2008), new Tiedtke ensemble cumulus scheme (Zhang et al., 2011), Yonsei University (YSU) planetary boundary layer (PBL) scheme with original MM5 scheme surface layer model (Hong et al., 2005), and the unified Noah land-surface model (Chen and Dudhia, 2001).

2.2. RAQMS

The Regional Air Quality Model System (named RAQMS) is a three-dimensional Eulerian model constructed on a spherical and terrain-following coordinate system. It contains a series of tropospheric physical and chemical processes of major chemical components, such as advection, diffusion, dry and wet deposition, and multiphase chemistry (An et al., 2002; Han et al., 2004; Han, 2007; Han et al., 2008a). Gas phase chemistry is represented by a chemical mechanism based on CBM-IV (the Carbon Bond Mechanism IV) (Gery et al., 1989). ISORROPIA model is applied to represent thermodynamic equilibrium processes of inorganic aerosols (Nenes et al., 1998). Secondary organic aerosol (SOA) formation is calculated with a four-bin volatility basis set (VBS) approach by considering oxidations of anthropogenic and biogenic volatile organic compounds, semi-volatile and intermediate volatile organic compounds (S/IVOCs), and subsequent partition into aerosol phase (Donahue et al., 2006; Han et al., 2016). Irreversible uptakes of glyoxal and methylglyoxal on wet aerosols and cloud droplets are also considered for SOA formation (Li et al., 2021). Aqueous chemistry and cloud microphysical modules are similar to those in RADM (Regional Acid Deposition Model) (Chang et al., 1987). Gas/particle mass transfer is represented by the CIT (the California/Carnegie-Mellon Institute of Technology) bulk equilibrium scheme (Meng et al., 1998). The optical properties of aerosols are mainly derived from the OPAC database (Optical Properties of Aerosols and Clouds) described in detail by Hess et al. (1998). The refractive index of mineral dust is retrieved from dust samples of Chinese deserts (Wang et al., 2004) instead of that in OPAC for deserts in other regions of the world. The major difference is the imaginary part of East Asian dust (0.004 at 0.5 μm) is smaller than that in the OPAC data set (0.008 at 0.5 μm), suggesting a larger single scattering albedo, which should be more realistic for mineral dust in East Asia. A Mie theory-based method (Ghan and Zaveri, 2007) is used to calculate aerosol optical parameters (extinction coefficient, single scattering albedo, and asymmetry factor). The κ-Köhler method (Petters and Kreidenweis, 2007) is adopted to calculate aerosol hygroscopic growth. An external mixing is assumed for dust and other aerosols, while anthropogenic aerosols are assumed to be internally mixed. Photolysis rates are calculated with the NCAR Tropospheric Ultraviolet–Visible (TUV) radiation model (Madronich and Flocke, 1999), which accounts for the impacts of clouds, aerosols, and gases on radiation. Anthropogenic aerosol is divided into two size sections, i.e., $PM_{2.5}$ (aerodynamic equivalent diameter below 2.5 μm), and $PM_{2.5–10}$ (aerodynamic equivalent diameter particles between 2.5 and 10 μm). Heterogeneous reactions on the surfaces of wet particles and cloud droplets are represented by the formula from Jacob (2000). Heterogeneous reactions on dust surfaces are treated mainly based on Li and Han (2010), with the heterogeneous reactions of HNO_3, SO_2 and N_2O_5 depending on RH (Tian et al., 2021b; Wagner et al., 2009). Heterogeneous reactions on dust are assumed to occur when calcium content exceeds sulfate and nitrate formed on dust, and the calcium content of dust is assumed to be 5 % by weight (Dentener et al., 1996). RAQMS

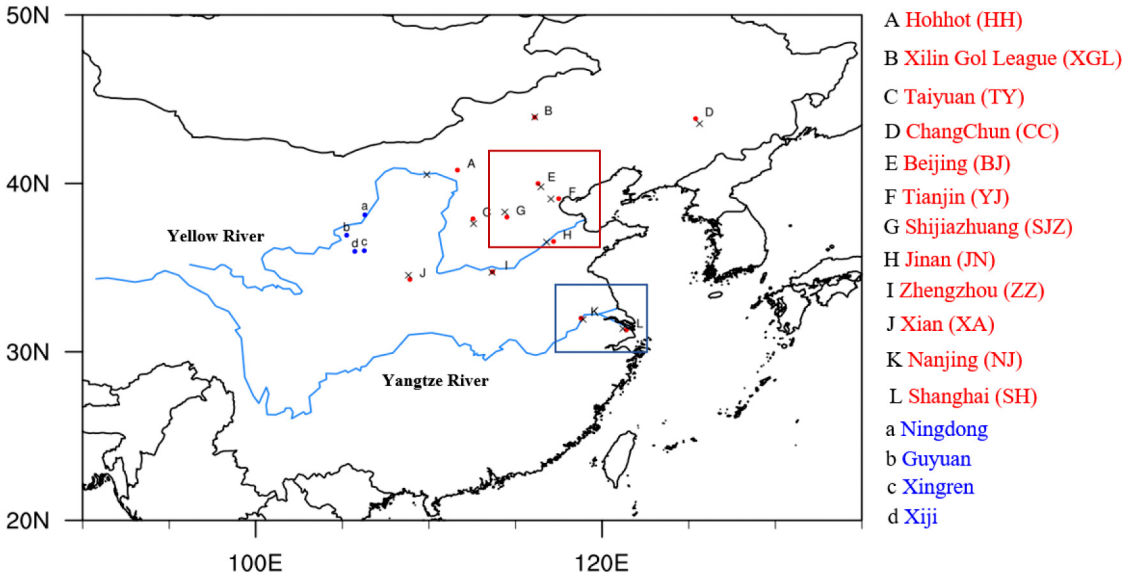

Fig. 1. The study domain, and the locations of 12 major cities (black cross denotes meteorological sites, red dot denotes air quality sites) and 4 monitoring sites for soil moisture (blue dot), red rectangle denotes the NCP region, black rectangle denotes the YRD region).

has participated in the Model Inter Comparison Study for Asia phase II (MICS-Asia II) project (Carmichael, 2008; Han et al., 2008a) and has been applied in previous studies on tropospheric ozone, acid deposition, aerosol pollution, and dust storm over East Asia (Han et al., 2006; Han et al., 2008b; Li et al., 2011; Li and Han, 2016; Li et al., 2018; Li et al., 2020; Li et al., 2021). More details on RAQMS refer to the references (Han et al., 2008a; Li and Han, 2016; Li et al., 2021).

2.3. Model configuration

The study domain is from 90° to 135°E and 20° to 50°N, including most areas of China (Fig. 1). The horizontal resolution is 0.5°, with twelve layers up to 10 km in the vertical and approximately seven layers in the boundary layer. The simulation period is from 00: 00 UTC on 05 March to 18: 00 UTC on 31 March 2021, with the first five days as initialization. Anthropogenic emission inventory with a horizontal resolution of 0.25° for March 2019 is derived from the Multi-resolution Emission Inventory for China (MEIC) (Zheng et al., 2021). This inventory for 2019 is assumed to represent emission status in 2021 in China considering the anthropogenic emission rebound in 2021 after the COVID-19 outbreak in January 2020. This inventory includes nine major species as sulfur dioxide (SO_2), nitric oxide (NO_x), non-methane volatile organic compounds (NMVOCs), carbonic oxide (CO), black carbon (BC), organic carbon (OC), ammonia (NH_3), primary $PM_{2.5}$ ($PPM_{2.5}$) and PMcoarse (refers to particles with an aerodynamic diameter of 2.5–10 μm) from five sectors, i.e., industry, transportation, agriculture, electric, power and residence. Primary S/IVOCs emissions over China are estimated based on primary organic aerosol (POA) emission from MEIC and based on the ratios of S/IVOCs to POA from previous publications (Pye and Seinfeld, 2010; Louvaris et al., 2017) for various anthropogenic sectors. Primary emissions of GLY and MGLY are also derived from MEIC, with the same grid resolution as other species. Monthly mean biomass burning emissions are derived from GFED (Global Fire Emission Database) (van der Werf et al., 2017) (http://www.globalfiredata.org/).

2.4. Observational data

China Meteorological Data Service Center (http://data.cma.cn) provides hourly observations of meteorological variables, including air temperature and relative humidity at 2 m (T2 and RH2), wind speed at 10 m (WS10), and precipitation. Observations in the 12 major cities of China (Fig. 1) are used for detailed model validation. High vertical resolution soundings of meteorological variables (temperature, relative humidity, and wind speed) are conducted every 1 s with the L-band sounding system at 8:00 LST on 15 March in Beijing by the China Meteorological Administration. Satellite retrievals of monthly accumulated precipitation with a spatial resolution of 0.1° are provided by the Global Precipitation Measurement (GPM) mission. Level 3 monthly precipitation product (GPM_3IMERGM) is used. Hourly observations for $PM_{2.5}$ and PM_{10} concentrations are derived from the Air Quality Database of the Ministry of Environmental Protection (http://datacenter.mep.gov.cn). Observations in the 12 major cities (same as those for meteorological observations) are used for detailed model validation and analysis. The observation for each of the 12 cities is an average of all monitoring sites in the city. Hourly concentrations of $PM_{2.5}$ chemical components are measured at the 325-m meteorological tower (116°22′E, 39°58′N) in the Tower branch of the Institute of Atmospheric Physics (IAP), which is located between the third and fourth ring roads in downtown Beijing. An Aerodyne time-of-flight aerosol chemical speciation monitor (ToF-ACSM) equipped with a capture vaporizer (CV) and $PM_{2.5}$ lens is used for measurement.

The latest land use data with a 500-meter resolution for 2020 is derived from the MODIS (Moderate Resolution Imaging Spectroradiometer) Land Cover Type Version 6 data product (MCD12Q1) (https://search.earthdata.nasa.gov/search). Soil texture map (including sand, silt, and clay contents with a 30 arcsec resolution) for China is provided by the Institute of Soil Science, Chinese Academy of Sciences and that for other countries is obtained from the Harmonized World Soil Database (HWSD; http://westdc.Westgis.ac.cn/data) released by the United States Department of Agriculture (USDA).

Soil moisture data is derived from AMSR2 (The Advanced Microwave Scanning Radiometer 2, https://search.earthdata.nasa.gov/search) onboard the GCOM-W1 (Global Change Observation Mission 1st-Water) satellite. In this study, daily ascending orbit data from 10 to 31 March 2021 with a spatial resolution of 10 km are used. Soil volume liquid water content at 0–10 cm soil depth is also measured by the DZN3 automatic soil water observation instrument (with an accuracy of 2.5 %; made by the China Huayun Group) at the four sites in Ningxia province (shown in Fig. 1).

AOD data at three sites in Beijing (Beijing:116.38°E, 39.98°N; CAMS:116.32°E, 39.93°N; RADI: 116.38°E, 40.01°N) and one site in Hebei province (Xianghe:116.96°E, 39.75°N) in the NCP region are obtained from the Aerosol Robotic Network (AERONET, https://aeronet.gsfc.nasa.gov/new_web/index.html). The satellite retrieved AOD at 550 nm at 13:30 LST is derived from the MODIS/Aqua Aerosol 5-Min L2 Swath 10 km product (MYD04_L2, https://search.earthdata.nasa.gov/). Vertical profile of aerosol extinction coefficient at 532 nm is derived from the LIDAR Level 2 Version 4.2 data production from CALIPSO (Cloud-Aerosol Lidar and Infrared Pathfinder Satellite Observations) (https://subset.larc.nasa.gov/calipso/), which is measured by the space-based lidar CALIOP (Cloud-Aerosol Lidar with Orthogonal Polarization) on board the CALIPSO satellite. Hourly shortwave radiation at the surface is measured at the Shangdianzi site (117.12°E, 40.65°N, 293 m above sea level, a remote site about 100 km northeast of Beijing) with the Kipp & Zonen CMP11 Pyranometer, and at the Xianghe site with the Eppley Normal Incidence Pyrheliometer and a Black &White pyranometer.

2.5. Dust model

The deflation, dry deposition and wet removals of dust particles are parameterized by Han et al. (2004). Particles with diameters ranging from 0.43 to 42 μm are divided into ten size bins (with size ranges in diameter being 0.43–0.65, 0.65–1.1, 1.1–2.1, 2.1–3.3, 3.3–4.7, 4.7–7.0, 7.0–11.0, 11.0–17.5, 17.5–27, 27–42 μm, respectively). Dry deposition velocity is represented by a size and land use dependent parameterization. Dry deposition velocity of particle is expressed as the inverse of the sum of resistances plus a gravitational settling term. Below-cloud scavenging of particles between cloud base and ground surface is parameterized as a function of precipitation rate and collision efficiency of particle by hydrometeor, which is also bin-resolved. Bare ground, bare ground with little shrub and grass are taken as potential dust deflation regions. Dust deflation is allowed in the above regions when near-surface friction velocity and relative humidity are larger and smaller than the threshold friction velocity and threshold relative humidity. The total dust emission flux is assigned to each size bin based on field measurements of size distribution of vertical dust flux over major Chinese deserts during the Aerosol Characterization Experiment–Asia (ACE-ASIA). More details refer to Han et al. (2004). The dust model exhibits a good ability in reproducing strong dust storms in past decades, such as the dust storms in the spring of 2002, 2006, 2009 and 2010 (Han et al., 2004; Li et al., 2011; Li and Han, 2015). However, in some dust storm cases, the model performance is not satisfactory, which could be attributed to potential uncertainties in land use and in controlling factors for dust deflation. Therefore, first, the dust model is developed by: 1) using the up-to-date land use data from MODIS retrievals for 2020 (Fig. S1) instead of the previous old land use data set; 2) introducing soil texture and soil moisture (Fig. S1) instead of relative humidity in calculation of threshold wind speed for dust deflation. Threshold friction velocity is calculated by threshold wind velocity according to Louis (1979). The fraction of clay in each model grid from the soil texture map is used to determine threshold soil moisture for calculating threshold wind speed, and a threshold soil moisture of 20 % is prescribed below which dust can be deflated based on Li et al. (2004). The dust model is incorporated into RAQMS to represent dust deflation, advection, diffusion, and deposition processes.

3. Results and discussions

3.1. Model validation

3.1.1. Meteorological variables

The WRF performance statistics for WS10, T2 and RH2 in the 12 cities are presented in Table S1. The overall meteorological predictions are generally satisfactory, with the correlation coefficient (R) and normalized mean bias (NMB) of 0.95 and −11.4 % for T2, 0.87 and −4.7 % for RH2, and 0.71 and 15.5 % for WS10 for all cities, respectively. However, WRF tends to predict higher wind speed in Shijiazhuang and Zhengzhou by 63 % and 66 %, respectively. Statistics are also calculated at 77 meteorological sites (including the 12 cities) over North and East China (shown in Table S2), which are similar to those in Table S1.

Fig. S2 presents the observed and WRF simulated vertical profiles of air temperature, wind speed, and relative humidity in Beijing at 08:00 LST on 15 March 2021, when the dust storm began to invade Beijing. In general, the model is able to capture the major features of vertical distribution of these meteorological variables. However, it is noteworthy that there are intense changes in the observed wind speed and relative humidity among different altitudes below 3 km, which are not well reproduced by WRF, suggesting potential underprediction of the strength of vertical wind shear and turbulent diffusivity. The overall statistics (Table S3) indicate that WRF predicts vertical profiles of meteorological variables generally well, with R above 0.9, and NMBs of −1.9 %, 12.7 %, and 3.5 % for wind speed, relative humidity, and air temperature, respectively.

The model comparison with the GPM data (Fig. S3) demonstrates that WRF is able to reproduce the major distribution features of precipitation, showing higher precipitation in the middle and lower reaches of the Yangtze River and portions of Northeast China, although low model biases exist in the NCP region and the lower reaches of the Yangtze River. Model results are also compared with surface precipitation observations at 77 meteorological sites (Table S2) of China, which shows a correlation coefficient of 0.66 for hourly precipitation and a NMB of −29.6 % for total precipitation, generally consistent with the low bias in WRF simulation in comparison with satellite retrievals.

Fig. S4 shows the retrieved soil moisture from AMSR2 data sets and from WRF simulation at 14:00 LST (the time of satellite passing over China) averaged over the study period. The model generally reproduces the spatial distribution of soil moisture in the domain except in portions of Northeast China and the NCP region, where WRF tends to predict lower soil moisture. Fig. S5 presents the measured and WRF simulated soil liquid water content at 0–10 cm soil depth at the four monitoring sites in Ningxia province of western China (Fig. 1), which are just

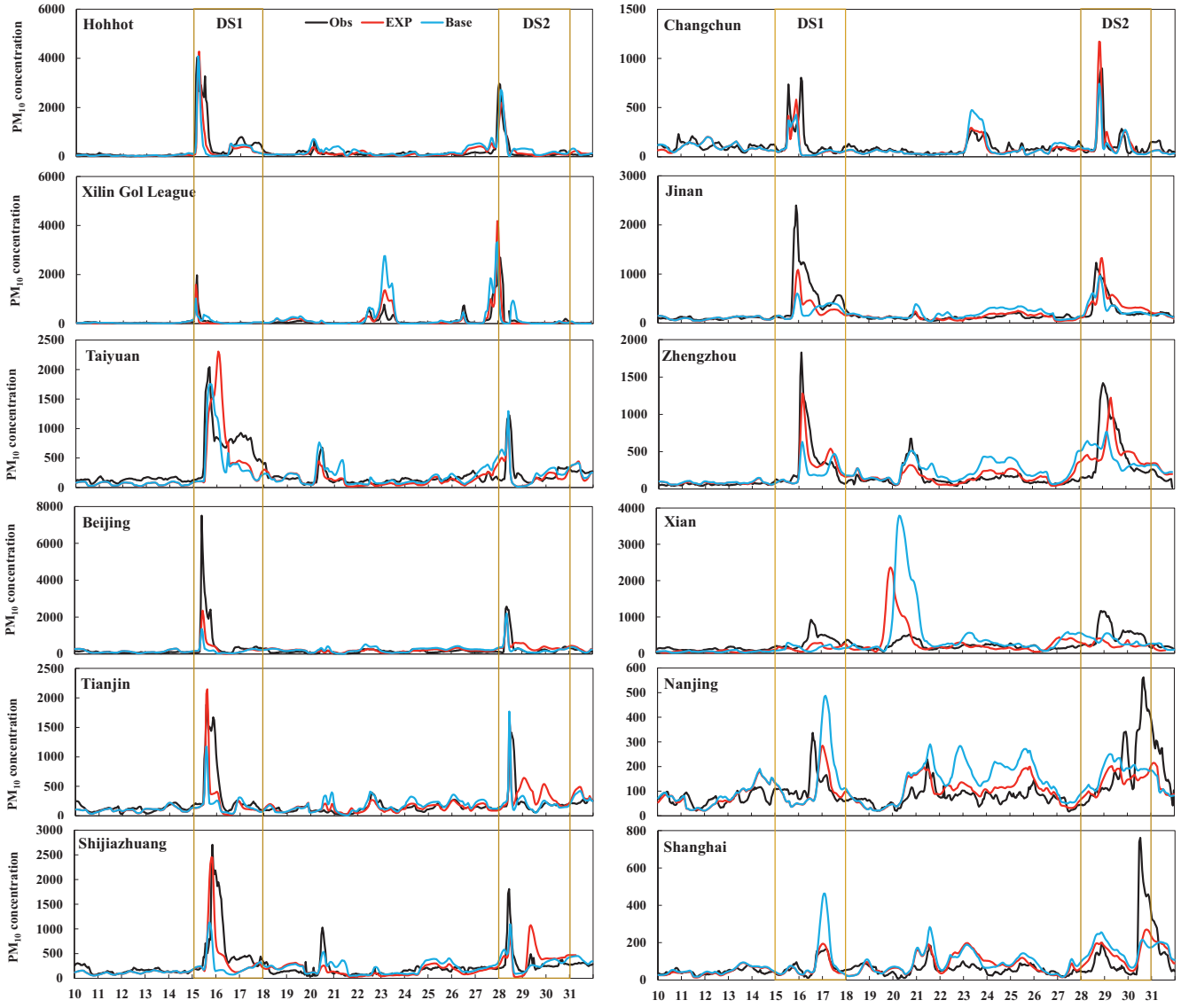

Fig. 2. Observed (black lines) and simulated hourly PM_{10} concentrations from the base case (blue line) and EXP case (red line) in the 12 cities on 10–31 March 2021 (μg m^{-3}).

downwind of the Gobi Desert. WRF reproduces the hourly variation of soil liquid water content quite well at the four sites, especially the fluctuation and decreasing trend during 19–23 March due to soil frozen and the abrupt increase on 31 March due to precipitation. The statistics for soil liquid water content are 0.47 for R, and 11.6 % for NMB for all sites (Table S4).

3.1.2. PM concentrations

Fig. 2 presents the observed and simulated hourly surface PM_{10} concentrations in the 12 major cities from North China to East China during the study period. There were two dust storms in March 2021, leading to the maximum hourly concentrations up to 7506 μg m^{-3} and 2568 μg m^{-3} in Beijing on 15 March (the first one refers to DS1) and on 28 March (the second one refers to DS2), respectively. DS1 is the severest dust storm since 2010. This dust storm was originated from southern Mongolia and influenced wide areas from the Gobi Desert to the middle and lower reaches of the Yellow River, Northeast China, the NCP region, and northern parts of the lower reaches of the Yangtze River.

Fig. 2 shows that both the base case (with the old dust model) and the EXP case (with the newly developed dust model by applying the up-to-date land use and by considering soil texture and soil moisture in the calculation of threshold friction velocity) can capture the two dust storms in these cities. The old dust model and the developed one both perform well in Hohhot and Xilin Gol League, which are close to the Gobi Desert. However, the developed dust model apparently improves PM_{10} simulation in downwind cities by: 1) enhancing the peak hourly PM_{10} values during DS1 in the major cities, for example, the simulated peak PM_{10} concentrations in Beijing, Tianjin, Shijiazhuang, and Zhengzhou increase from 1359.2 μg m^{-3}, 1175.1 μg m^{-3}, 1131.4 μg m^{-3}, 632.8 μg m^{-3} in the base case to 2355.1 μg m^{-3}, 2147.1 μg m^{-3}, 2450.3 μg m^{-3}, 1280.6 μg m^{-3} in EXP, respectively, apparently closer to the observations of 7506.3 μg m^{-3}, 1886.9 μg m^{-3}, 2704 μg m^{-3}, 1829.9 μg m^{-3} in the 4 cities. 2) reducing the overprediction of PM_{10} concentration (or removing 'fake' dust event) during non-dust or weak dust periods, especially in the downwind cities of East China during 20–26 March, e.g., the overestimations in Zhengzhou and Nanjing are reduced from 260.8 μg m^{-3} and 177.7 μg m^{-3} to 155.5 μg m^{-3} and 122.1 μg m^{-3} on average, closer to the observations of 152.4 μg m^{-3} and 84.5 μg m^{-3}, respectively. Besides, the overestimations of PM_{10} concentrations caused by dust aerosols are also reduced in Xilin Gol League, Changchun, Jinan, and Shanghai during 20–26 March. Both the old and new dust models reproduce the PM_{10} peaks during DS2 quite well in most of the cities, but the improvement by the new model for PM_{10} peaks in DS2 is relatively small compared with that in DS1 except for the apparent increases in peak PM_{10} concentrations in Jinan and Zhengzhou on 29 March. It is noteworthy that PM_{10} concentration in Beijing is largely underpredicted on 15 March during DS1. Although the developed dust model apparently improved PM_{10} simulation by increasing the hourly peak value to 2355 μg m^{-3} from 1359 μg m^{-3} in the base case, it is still lower than the observed peak of 7506 μg m^{-3}. As described above, the intense variation in vertical wind speed cannot be well reproduced by WRF simulation, which could lead to weaker wind shear and vertical diffusivity. Our analysis is proved by a recent study for the same dust storm period on 15 March (Zhang et al., 2022), in which they analyzed two-layer atmospheric measurements at the 325-m meteorological tower in Beijing and found a rapid turbulence burst as a cold front along with DS1 approached Beijing at about 08:00 LST on 15 March, which efficiently mixed abundant dust particles aloft downward to the ground surface. The estimated turbulent kinetic energy below 280 m from Zhang et al. (2022) is approximately 5–10 times higher than the WRF simulated corresponding values in this study, which can explain the lower PM_{10} simulation than observation on 15 March, that is the simulated weaker vertical mixing of dust aloft to the ground surface.

The model performance statistics for PM_{10} concentration are presented in Table 1. For the dust storm episodes (DS1 and DS2), it is evident that the EXP case with the developed dust model yields better statistics in comparison with observations, with R of 0.71 and NMB of −20 %, compared with R of 0.58 and NMB of −26 % in the base case. For the entire study period including both dust and non-dust periods, the correlation coefficient is also apparently enhanced from 0.48 in the base case to 0.69 in EXP. The slight increased NMB from 2.9 % to −8.1 % in EXP can be explained by the underprediction during non-dust periods, which could be due to potential underestimation of anthropogenic emissions.

Table 1
Model performance statistics for hourly near-surface PM_{10} concentrations from EXP in the megacities of China during 10–31 March 2021 (statistics in brackets are for the two dust storm periods, city abbreviation refers to Fig. 1).

Cities		C_{obs} (μg m^{-3})	C_{sim} (μg m^{-3})	R	MB	NMB (%)
HH		239.4	191.6	0.81	−47.9	−19.9
XGL		116.1	123.3	0.78	7.2	6.2
TY		252.4	200.9	0.69	−51.5	−20.4
CC		109.3	90.5	0.68	−18.8	−17.2
BJ		240.8	222.5	0.81	−18.4	−7.6
TJ		191.6	182.7	0.66	−8.9	−4.6
SJZ		258.5	231.2	0.65	−27.3	−10.6
JN		221.8	187.4	0.76	−34.4	−15.5
ZZ		211.6	216.6	0.82	5.0	2.4
XA		247.6	221.6	0.30	−26.0	−10.5
NJ		102.6	102.3	0.49	−0.3	−0.3
SH		75.7	85.3	0.65	9.6	12.7
All	EXP	184.9	169.9	0.69	−14.9	−8.1
				(0.71)	(−63.6)	(−20.2)
	Base		190.2	0.48	5.3	2.9
				(0.58)	(−81.1)	(−25.8)

Table 2 shows the simulated and observed near surface $PM_{2.5}$ concentrations and performance statistics. In all, the model generally reproduces the hourly variation of $PM_{2.5}$ concentrations in the EXP case, with an overall R of 0.55 and NMB of 14.8 %. The correlation coefficients range from 0.50 to 0.80 in the upwind regions (Hohhot, Xilin Gol League, Taiyuan, Changchun), 0.54–0.67 in the NCP region (Beijing, Tianjin, Shijiazhuang, Jinan, Zhengzhou), and 0.38–0.61 in the YRD region (Nanjing, Shanghai). The positive model biases by 33–62 % in Zhengzhou, Jinan, Shijiazhuang, and Nanjing could be associated with potential uncertainties in anthropogenic emissions in these regions. The model performances in Beijing and Tianjin are generally satisfactory, with R above 0.60 and NMB within 20 %. Statistics for PM_{10} and $PM_{2.5}$ are also calculated at 864 air quality sites (including the 12 cities) over North and East China (shown in Table S2, simulation is from the EXP case), which are similar to those in Table 1 and Table 2.

3.1.3. Aerosol chemical components

Fig. 3 shows the simulated (from EXP) and observed hourly concentrations of $PM_{2.5}$ and its chemical components in Beijing. Besides the two dust storms, there were two haze episodes, on 10–14 March, and on 26–27 March, with the peak $PM_{2.5}$ values of 276 μg m^{-3} and 193 μg m^{-3}, respectively. During DS1, the observed peak $PM_{2.5}$ concentration reached 742 μg m^{-3}, somewhat higher than the simulated 564 μg m^{-3}. In general, the model reproduces the evolution of $PM_{2.5}$ and its chemical components

Table 2
Model performance statistics for hourly near-surface $PM_{2.5}$ concentrations from EXP in megacities of China during 10–31 March 2021 (city abbreviation refers to Fig. 1).

Cities	C_{obs} (μg m^{-3})	C_{sim} (μg m^{-3})	R	MB	NMB (%)
HH	75.9	55.5	0.68	−20.4	−26.9
XGL	24.6	28.1	0.80	3.5	14.0
TY	92.2	73.0	0.50	−19.1	−20.8
CC	52.3	52.6	0.56	0.30	0.6
BJ	84.9	98.0	0.60	13.2	15.5
TJ	72.8	86.5	0.63	13.7	18.8
SJZ	80.6	108.3	0.54	27.7	34.3
JN	64.6	88.3	0.58	23.7	36.7
ZZ	66.3	87.8	0.67	21.5	32.5
XA	67.0	82.3	0.15	15.3	22.9
NJ	40.6	65.6	0.38	25.1	61.8
SH	42.1	50.9	0.61	8.8	20.8
All	63.7	73.1	0.55	9.4	14.8

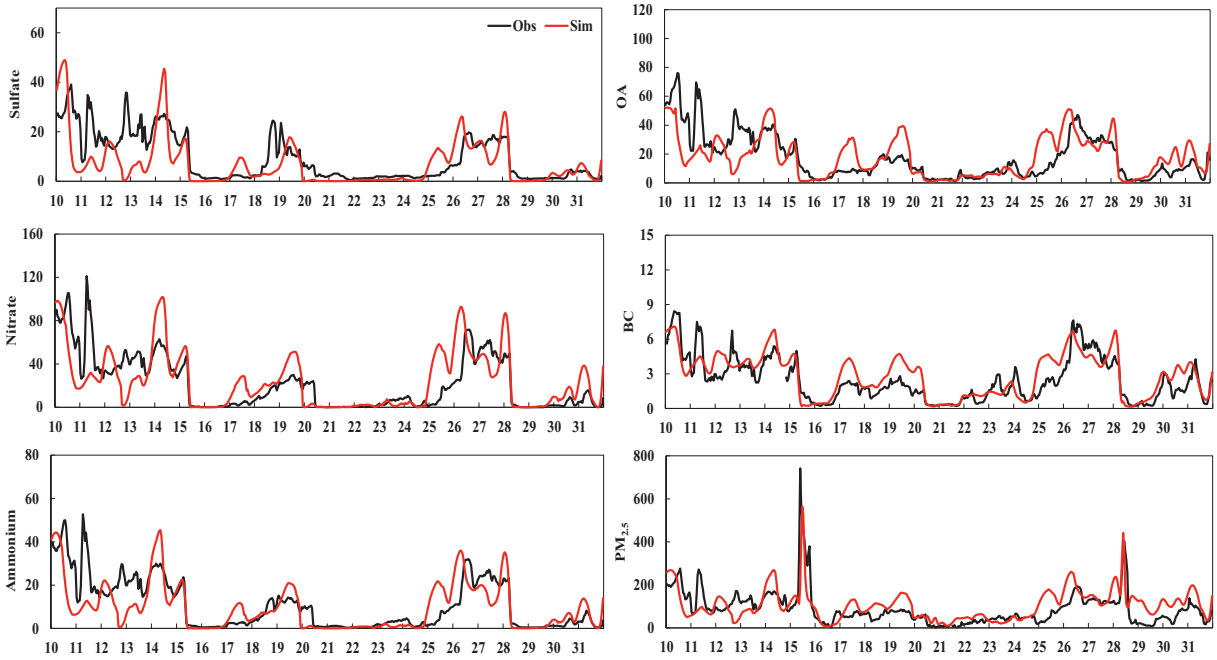

Fig. 3. The observed and model simulated (from the EXP case) hourly concentrations of $PM_{2.5}$ and its chemical components in Beijing on 10-31March 2021 (unit: μg m^{-3}).

quite well, although inorganic aerosol concentrations are somewhat underpredicted on 11–13 March during the first haze episode. The overall model performances for $PM_{2.5}$ chemical components are generally good (Table 3), with Rs of 0.63, 0.69, 0.70, 0.81, 0.61 and NMBs of −23.1 %, 11.5 %, −10.4 %, 17.2 %, 2.2 % for sulfate, nitrate, ammonium, BC, and OA, respectively.

3.1.4. AOD and aerosol extinction coefficient

Fig. 4 shows the measured and simulated hourly AOD at the four AERONET sites during the study period. In general, the model reasonably reproduces the hourly variation of AOD at these sites around Beijing. However, the model tends to underpredict observation during the first haze episode, which is mainly due to the underprediction of inorganic aerosol concentrations discussed above (Fig. 3). Unfortunately, measurements are not available on 15 March during DS1. The model generally reproduces AOD variation and magnitude, with an overall R of 0.52 and NMB of −16.7 %, respectively, for all the 4 sites (Table 4).

Fig. 5 shows the distribution of AOD retrieved from MODIS and from the EXP simulation at 13:30 LST on 14–15, and 27–28 March during the two dust storms. At 13:30 LST on 14 March, high MODIS retrieved AOD up to 2.5 occurred over the Gobi Desert of southwestern Mongolia (Fig. 5a), which was also reproduced by the model, with AOD approaching 2.0 (Fig. 5e). MODIS data was not available over wide downwind areas including the NCP at this time. Fig. 5b shows a long belt with high AOD up to 5.0 spanning from western China, to the NCP and the Bohai Bay at 13:30 LST on 15 March, although the MODIS data was not continuous in Northeast China and the NCP due to cloud screening. The model correctly reproduces this spatial distribution pattern, in particular, the model well captures the retrieved high AOD around 5.0 over the Bohai Bay (Fig. 5f). MODIS AOD was as high as 2.8 in the vicinity of southeastern China-Mongolia border at 13:30 LST on 27 March due to the second dust storm (Fig. 5c). The model generally reproduces the distribution and magnitude of the observed AOD (Fig. 5g). At 13:30 LST on 28 March, the model results show a long belt with elevated AOD extending from the Bohai Bay to the northmost forest areas of Northeast China, resulting from the eastward transport of the second dust storm (Fig. 5h), generally consistent with the MODIS AOD, although the satellite data are absent in the northern parts of Northeast China due to cloud effect (Fig. 5d).

Fig. S6 shows the CALIPSO retrieved (at 532 nm) and model simulated vertical profiles of aerosol extinction coefficient (550 nm) during the two dust storms. At 13:17 LST on 15 March, CALIPSO satellite passed over East China from the YRD to NCP regions (Fig. S6a). The first dust storm arrived at Beijing at about 08:00 LST on 15 March. At 13:17 LST, the dust plume moved to the eastern part of the NCP region and the Bohai Bay and was captured by CALIPSO, showing elevated extinction coefficients at altitudes of approximately 2 km around 38°N and 42°N (data are unavailable in the surrounding areas due to cloud) (Fig. S6b). The model reasonably reproduces the locations and magnitudes of high extinction coefficients in these regions (Fig. S6c). At the midnight of 28 March during the second dust storm, CALIPSO crossed the NCP (Fig. S6d) and captured the enhanced extinction coefficient exceeding 1.0 at latitudes from 35°N to 40°N (Fig. S6e). The model results agree with the satellite retrievals quite well in these regions and exhibit high extinction coefficients north of 40°N, which are mainly contributed by the dust storm transported over Northeast China (Fig. S6f). In all, RAQMS is capable of reproducing the spatial and vertical distribution and evolution of the two dust storms in comparison with satellite retrievals.

Table 3
Model performance statistics for hourly $PM_{2.5}$ chemical components from EXP in Beijing during 10–31 March 2021.

	SO_4^{2-}	NO_3^-	NH_4^+	BC	OA
C_{obs} (μg m^{-3})	9.1	21.3	10.5	2.4	17.2
C_{sim} (μg m^{-3})	7.0	23.8	9.4	2.9	17.6
R	0.63	0.69	0.70	0.81	0.61
MB (μg m^{-3})	−2.1	2.4	−1.1	0.4	0.4
NMB (%)	−23.1	11.5	−10.4	17.2	2.2

3.1.5. Total shortwave radiation flux

Fig. 6 presents the observed and model simulated (from EXP) hourly downward shortwave radiation at the surface (SWDOWN) at the Shangdianzi and Xianghe sites. In general, the model is able to reasonably reproduce SWDOWN during the study period, although there are some overpredictions in some days, e.g., 12, 26, and 28 March at Shangdianzi, and 12, 14, and 27 March at Xianghe, which can be mainly attributed to the underprediction of cloud amount by WRF (Figure not shown). It is encouraging that the model well captures the decreases in SWDOWN both

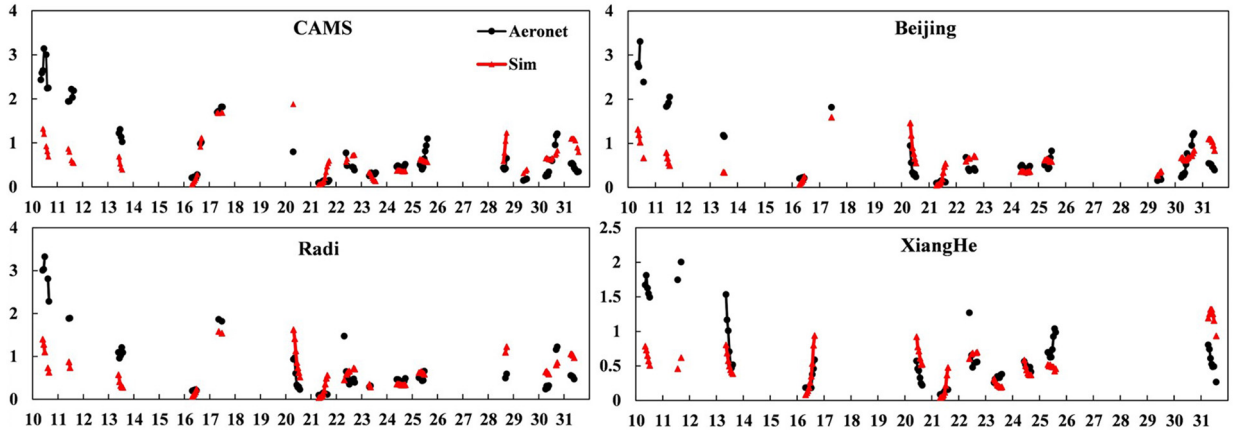

Fig. 4. The model simulated (from EXP) and observed hourly AOD (at 550 nm) at the four sites of AERONET on 10-31March 2021.

at Xianghe and at Shangdianzi on 15 March while the first dust storm arrived, the predicted higher SWDOWN at Xianghe could be associated with the underprediction of peak PM_{10} concentration as shown in Beijing (Fig. 2) discussed above. It is interesting to note that the model bias in surface SWDOWN is much less than the model bias in surface peak PM_{10} concentration on 15 March in Beijing, which implies that the model prediction of column PM_{10} concentration could be reasonable because surface radiation is affected by attenuation of all aerosols in the vertical column. The model slightly overpredicts surface SWDOWN on 28 March during the second dust storm at both sites, which could be due to potential underprediction of cloud amount. The overall performance statistics for surface SWDOWN at the Xianghe and Shangdianzi sites are 0.92 and 0.94 for R, 18.5 % and 21.5 % for NMB, respectively, indicating a generally good model ability in reproducing surface SWDOWN variation and magnitude.

4. Model results

4.1. Dust emission and transport

Fig. 7 shows the surface weather maps (from the National Meteorological Centre, http://www.nmc.cn/), dust emission fluxes, and surface dust concentrations on 14, 15, 16, and 27 March 2021, representing the time periods during the two dust storms. At 14:00 LST on 14 March 2021, a strong Mongolian cyclone with a cold front passed through Mongolia, and wind speeds over eastern Mongolia in front of the Mongolian cyclone reached 18 m s^{-1} (Fig. 7a). Dust emission flux reached as high as 2785 μg m^{-2} s^{-1} in southern Mongolia, with the maximum dust concentration up to 18,000 μg m^{-3} in the same region (Fig. 7e, i). At 08:00 LST on 15 March, the cyclone moved to Northeast China (Fig. 7b), driving dust plumes southward with the front edge reaching the northern parts of the NCP, meanwhile, there were some dust deflations over the deserts in the vicinity of southern China-Mongolia border (Fig. 7f), leading to an increase in dust concentration exceeding 10,000 μg m^{-3} in those areas (Fig. 7j). At 20:00 LST on 16 March, the cold front moved further to the south, and the high-pressure center behind the front gradually weakened and moved to the Bohai Bay. As a result, a clockwise circulation appeared there and blew dust particles to mainland China (Fig. 7k). Such backflow transport characteristics were well captured by the model, which led to an increase in PM_{10} concentrations in Beijing, Tianjin, and Shijiazhuang on 16–17 March (Fig. 2). At this time, dust particles were also transported to the YRD region, leading to an increase in PM_{10} level on 16–17 March in Nanjing and Shanghai as well (Fig. 2). At 14:00 LST on 27 March, a cyclone occurred in southeastern Mongolia (Fig. 7d), resulting in dust deflation again and generating the second dust storm. The maximum dust emission flux reached 1200 μg m^{-2} s^{-1} (Fig. 7h), lower than that on 14 March during DS1 (Fig. 7e). The center of high dust concentration during this dust storm was located in southeastern Mongolia, with the maximum exceeding 10,000 μg m^{-3} (Fig. 7l), also lower than that during the first dust storm (Fig. 7i). This dust storm moved southeastward as shown in Fig. 5h.

Table 4
Model performance statistics for hourly-mean AOD at the four sites of AERONET in the NCP region during 10–31 March 2021.

	Obs	Sim	R	MB	NMB
CAMS	0.77	0.60	0.56	−0.17	−22.1 %
Beijing	0.68	0.57	0.50	−0.11	−16.0 %
Radi	0.72	0.60	0.69	−0.12	−17.8 %
Xianghe	0.60	0.52	0.36	−0.08	−13.4 %
All	0.70	0.58	0.52	−0.11	−16.7 %

4.2. Impacts of dust on shortwave radiation and atmospheric chemistry

Considering the first dust storm is stronger than the second one, the following analysis focuses on the first dust storm on 14–17 March 2021.

4.2.1. Impact of dust on shortwave radiation

Fig. 8 presents the simulated changes in shortwave radiation at the surface due to attenuation by mineral dust during the first dust storm. At 10:00 LST on 15 March, when the first dust storm arrived in Beijing, surface shortwave radiation was reduced by a long belt of dust plumes extending from western Inner Mongolia, the middle reaches of the Yellow River, to the NCP and Northeast China, with the maximum decrease exceeding 400 W m^{-2} (>70 %) in central Northeast China (Fig. 8a). At this time, the simulated surface shortwave flux decreased by 313 W m^{-2} (72 %) in Beijing. Averaged over the DS1 period, dust aerosol exerted a consistent reduction in daytime surface shortwave radiation over wide areas from the Gobi Desert to wide areas of East China north of the Yangtze River, including the NCP region, with the maximum decrease of 189 W m^{-2} (45 %) over the deserts near the southern China-Mongolia border (Fig. 8b). The NCP region and northern YRD experienced surface shortwave radiation reductions of ~140 W m^{-2} (~35 %) and ~ 60 W m^{-2} (~10 %), respectively (Fig. 8b). In terms of domain average, the surface shortwave radiation reductions by dust aerosol extinction are estimated to be 62 W m^{-2} (16 %) and 17 W m^{-2} (4 %) over the NCP and YRD regions, respectively, during the first dust storm episode.

4.2.2. Dust effect on photolysis and photochemistry

Dust aerosols can weaken photolysis rate by attenuation of solar radiation, consequently affecting radical abundance, oxidation capability and secondary aerosol formation. To address this effect, a sensitivity simulation based on the EXP experiment is conducted by setting dust extinction coefficient to zero in the TUV model, and the difference between the sensitivity

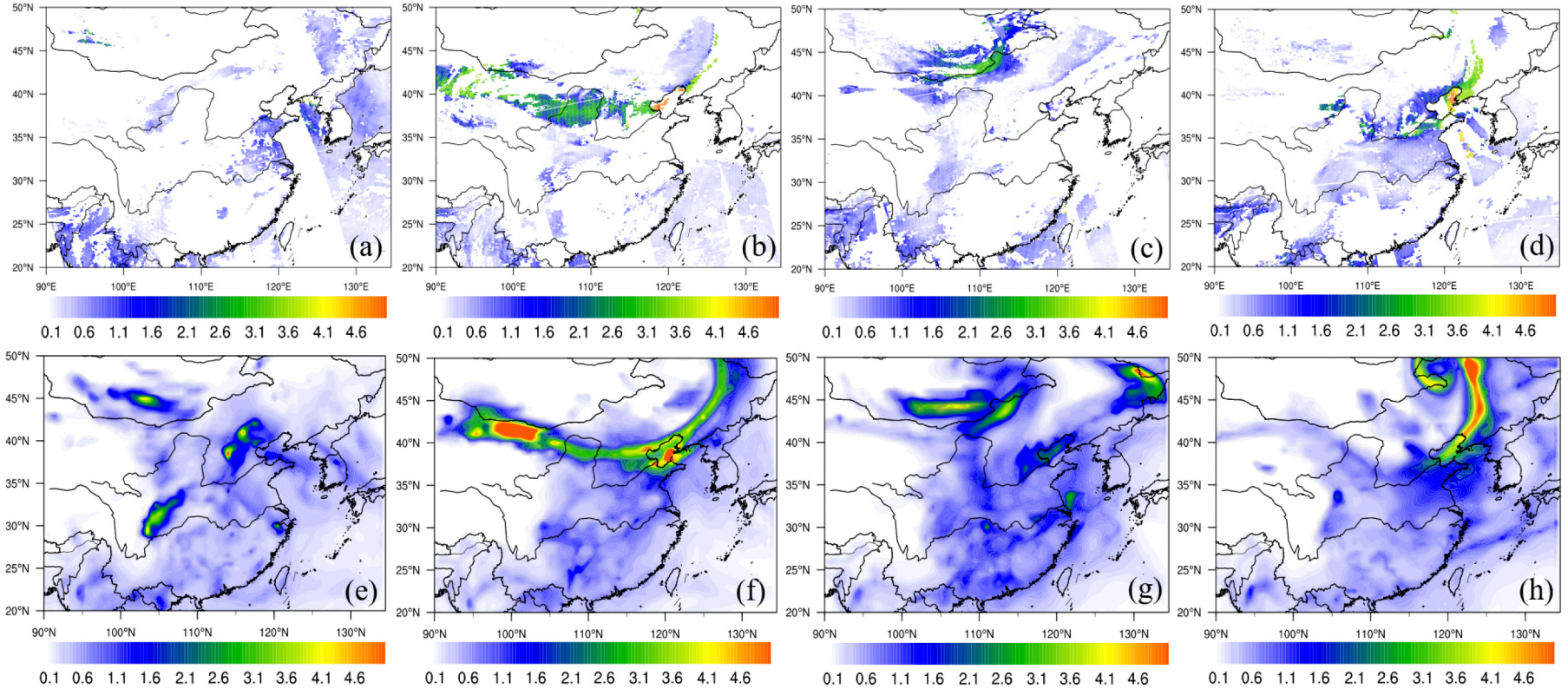

Fig. 5. AOD at 550 nm at 13:30 LST from (a-d) MODIS and (e-h) model simulations, on (a)(e) 14 March, (b)(f) 15 March, (c)(g) 27 March, (d)(h) 28 March 2021.

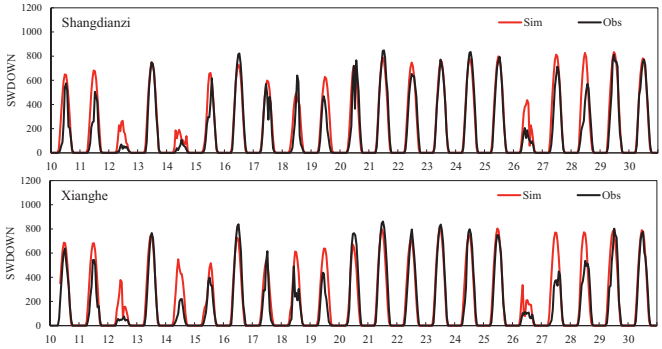

Fig. 6. The model simulated (from EXP) and observed surface hourly shortwave radiation at the Shangdianzi and Xianghe sites (unit: W m^{-2}).

case and EXP reflects the effect of dust aerosol on photolysis rate and photochemistry.

Fig. S7 shows the daytime (from 7:00 to 18:00 LST) average changes in surface photolysis rates of O_3 ($j[O_3]$) and NO_2 ($j[NO_2]$) due to dust effect on radiation during 14–17 March. Dust extinction of shortwave radiation led to reductions in $j[O_3]$ by up to 1.8×10^{-6} s^{-1} (32 %) over the Gobi Desert of western China, and by up to 1.0×10^{-6} s^{-1} (25 %) in the NCP region. The areas with the maximum reduction in j $[NO_2]$ were similar to those in j $[O_3]$, with the maximum reduction of 2.0×10^{-3} s^{-1}. The lower reaches of the Yellow River also experienced an apparent photolysis rate decrease by 1.1×10^{-3} s^{-1} (15 %), which could be attributed to the effect of dust backflow discussed above.

Fig. 9 shows the daytime mean changes in chemical component concentrations caused by the reduced photolysis rate during the first dust storm on 14–17 March. It is evident that dust particles reduced OH concentration by $\sim 1.0 \times 10^{-5}$ ppb (~25 %) in the Gobi Desert, most areas of North China and Northeast China mainly due to the reduction in O_3 photolysis (Fig. 9a). Because the photolysis rate of NO_2 was weakened (Fig. S7b), NO_2 increased slightly by ~0.6 ppb (3 %) mainly over the NCP region (Fig. 9b). In response to the decreased NO_2 photolysis, O_3 concentration decreased by ~1.8 ppb (10 %) in the NCP region (Fig. 9c). It is noted that total sulfate TSO_4^{2-} (including sulfate in the atmosphere and formed on dust surface), total nitrate TNO_3^- (including nitrate in the atmosphere and formed on dust surface) and SOA consistently decreased by ~0.08 μg m^{-3} (~1 %), ~1.4 μg m^{-3} (~3 %), and ~1.0 μg m^{-3} (~7 %), respectively, in the NCP region (Fig. 9d,e,f), which were mainly due to the decreasing OH level and weakened oxidation of SO_2, NO_2 and VOC by OH radical. Total sulfate concentration was found to increase slightly in some areas, which could be explained by potentially enhanced sulfate formation through dust heterogeneous reactions due to increasing SO_2 in the atmosphere (Figure not shown) by weakened reaction with OH radical discussed above.

4.2.3. Impact of dust heterogeneous reactions on chemical species

A sensitivity case without heterogeneous reactions on dust surface based on the EXP case is conducted to identify the impact of heterogeneous reactions on gases and aerosol chemical components during the first dust storm episode.

Fig. 10 shows the changes in concentrations of major gases and secondary aerosols. Fig. 10a shows that SO_2 concentration decreased by 0.4 ppb (5 %) mainly in the middle reaches of the Yellow River,

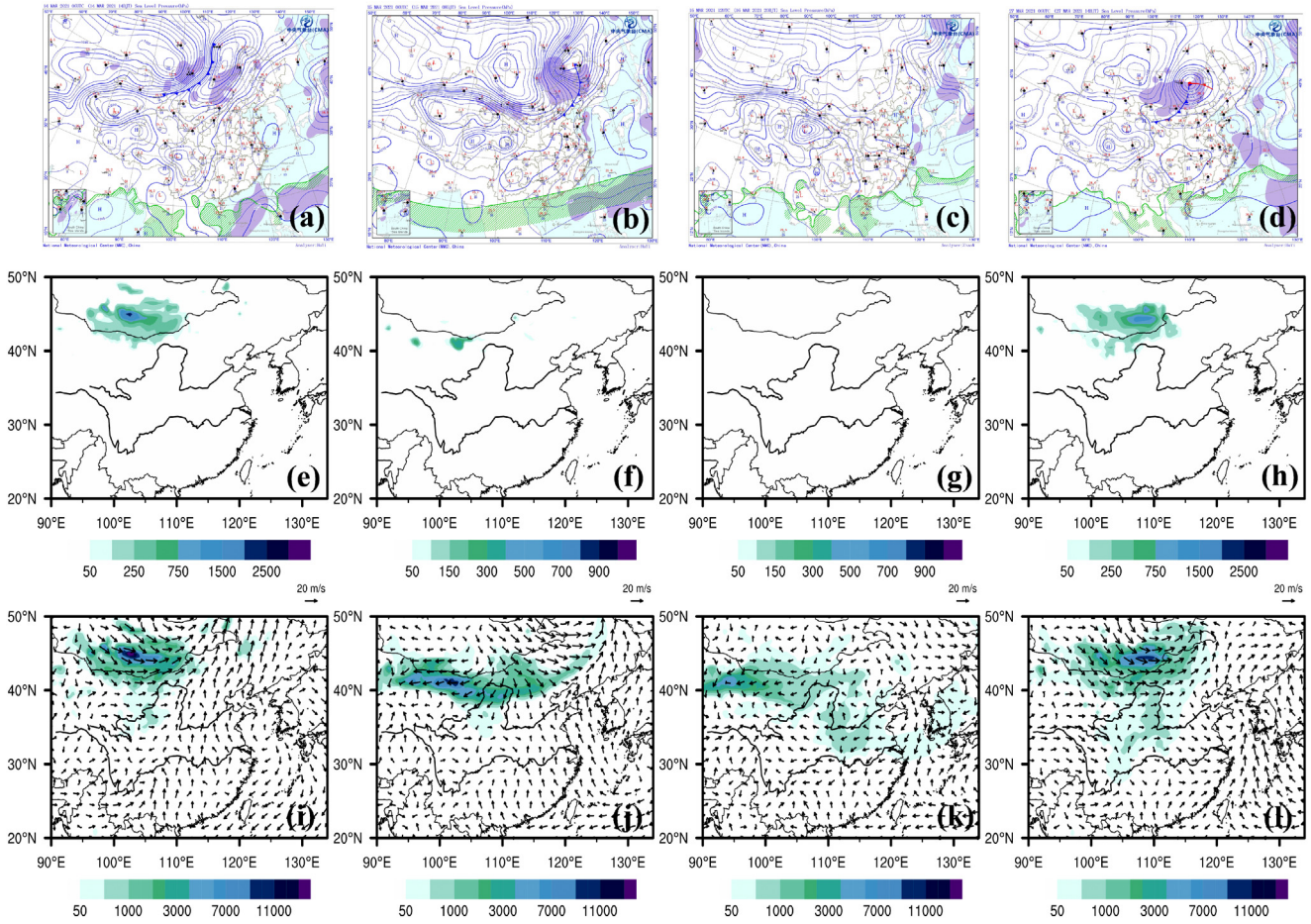

Fig. 7. Surface weather maps (a) at 14:00 LST on 14 March, (b) at 08:00 LST on 15 March, (c) at 20:00 LST on 16 March, and (d) at 14:00 LST on 27 March; (e)-(h) corresponding model simulated dust emission fluxes (unit: μg m^{-2} s^{-1}); (i)-(l) simulated near surface dust concentrations (with wind vector) (unit: μg m^{-3}).

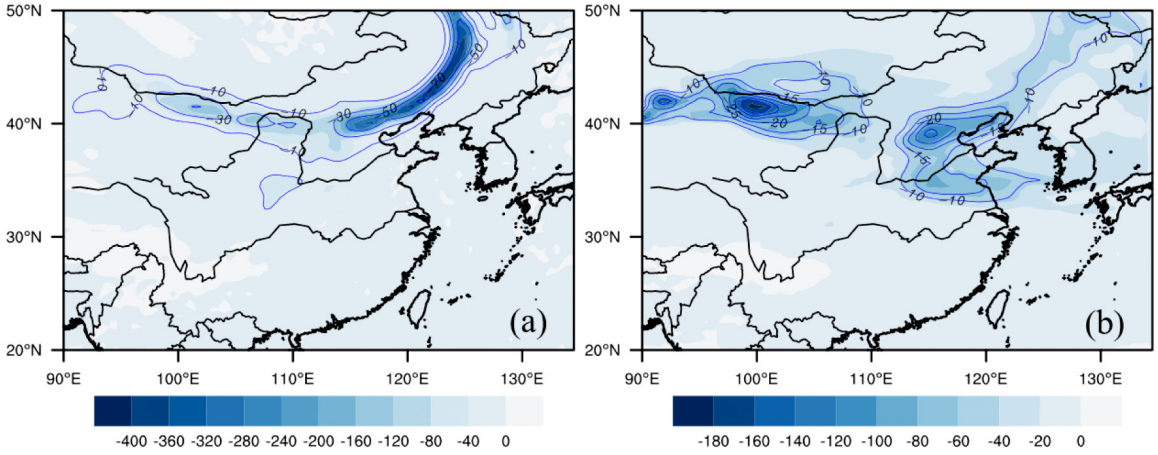

Fig. 8. The model simulated changes in (a) surface shortwave radiation at 10:00 LST on 15 March, (b) daytime average surface shortwave radiation over 14–17 March (unit: W m^{-2}) (Contour denotes percentage change, unit: %).

where both dust loading and anthropogenic SO_2 concentration and relative humidity were high and conducive to heterogeneous reactions.

NO_2 concentration decreased by 0.5 ppb (2 %) mainly over the NCP region (Fig. 10b) with high NO_x emission, due to loss on dust surface, whereas O_3 decreased by up to 20 ppb (30 %) in the Gobi Desert because of the high dust loading and O_3 concentration there (Fig. 10c). Total sulfate and nitrate consistently increased by ~1.6 μg m^{-3} (30 %) and ~ 6 μg m^{-3} (20 %) in the middle reaches of the Yellow River (Fig. 10d,e), mainly due to the increases in sulfate and nitrate formed on dust surface, whereas sulfate (SO_4^{2-}) and nitrate (NO_3^-) in the atmosphere decreased by 0.3 μg m^{-3} (5 %) and 5 μg m^{-3} (20 %) in the similar areas of total sulfate and nitrate increase because of less SO_2 and NO_2 in the atmosphere due to the heterogeneous reactions.

Ammonium concentration decreased by ~1.8 μg m^{-3} (15 %) in the middle reaches of the Yellow River and portions of central China between the Yellow River and the Yangtze River, which was attributed to the decreasing SO_2 and NO_2 in the atmosphere due to heterogeneous reactions (Fig. 10f). It is noted that SOA concentration increased by ~0.35 μg m^{-3} (~1 %) in the lower reaches of the Yellow River, which was due to more oxidation of VOC by increasing OH radical due to oxidation of less SO_2 and NO_2 in the atmosphere discussed above.

It is interesting to note that the intensity of heterogeneous reactions on dust surfaces varied largely with dust evolution. When the first dust storm began to sweep over the NCP region on 15 March, productions of sulfate and nitrate through heterogeneous reactions on dust surfaces were limited because strong wind with cold front swept away SO_2 and NO_2, leaving little gas precursors to react on dust surfaces, thus there were only 3.1 % and 1.7 % increases in sulfate and nitrate through heterogeneous reactions in the NCP region. However, during the dust backflow period on 16–17 March (Fig. 7k) under moderate east and south winds with increasing relative humidity (from 28 % on 15 March to 37 % on 16–17 March in terms of NCP average), higher SO_2 and NO_2 concentrations in the NCP reacted with the backflow dust plumes more intensely, resulting in apparent increases in sulfate and nitrate concentration by 18.2 % and 23.8 % on average in the NCP, respectively (Fig. S8).

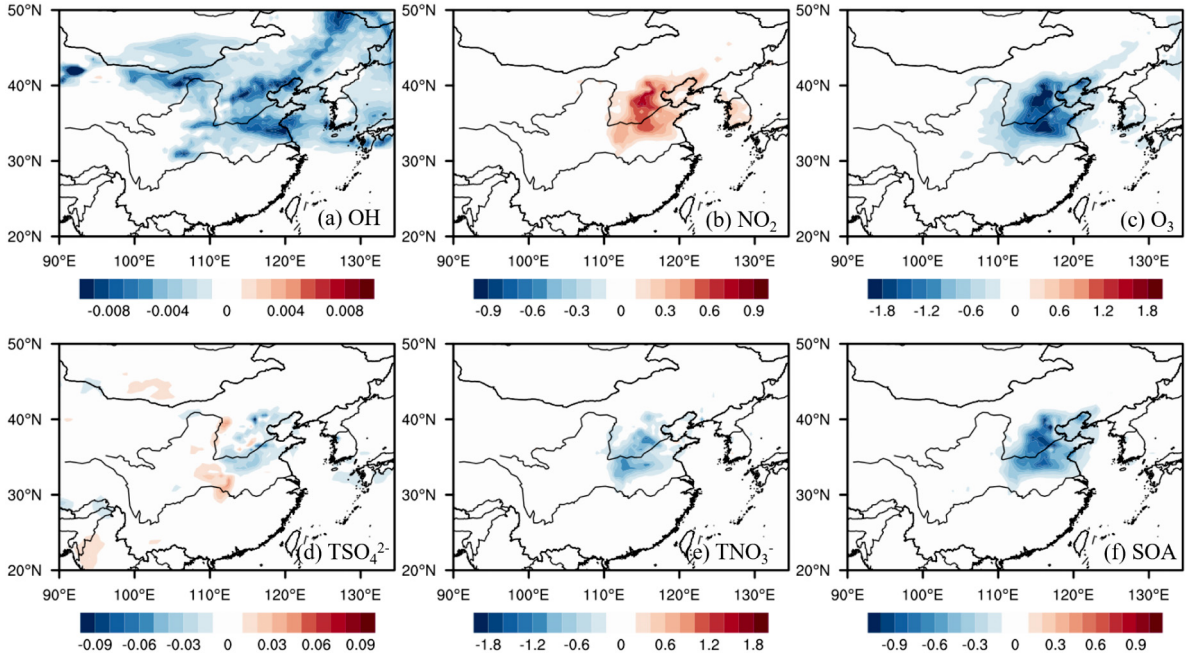

Fig. 9. The simulated daytime mean changes in (a) OH, (b) NO_2, (c) O_3, (d) TSO_4^{2-}, (e) TNO_3^-, (f) SOA concentrations during 14–17 March (DS1) due to photolysis rate change (units: ppt for OH, ppb for NO_2 and O_3, μg m^{-3} for aerosols). Note TSO_4^{2-} and TNO_3^- denote total sulfate and total nitrate formed in the atmosphere and on dust surface.

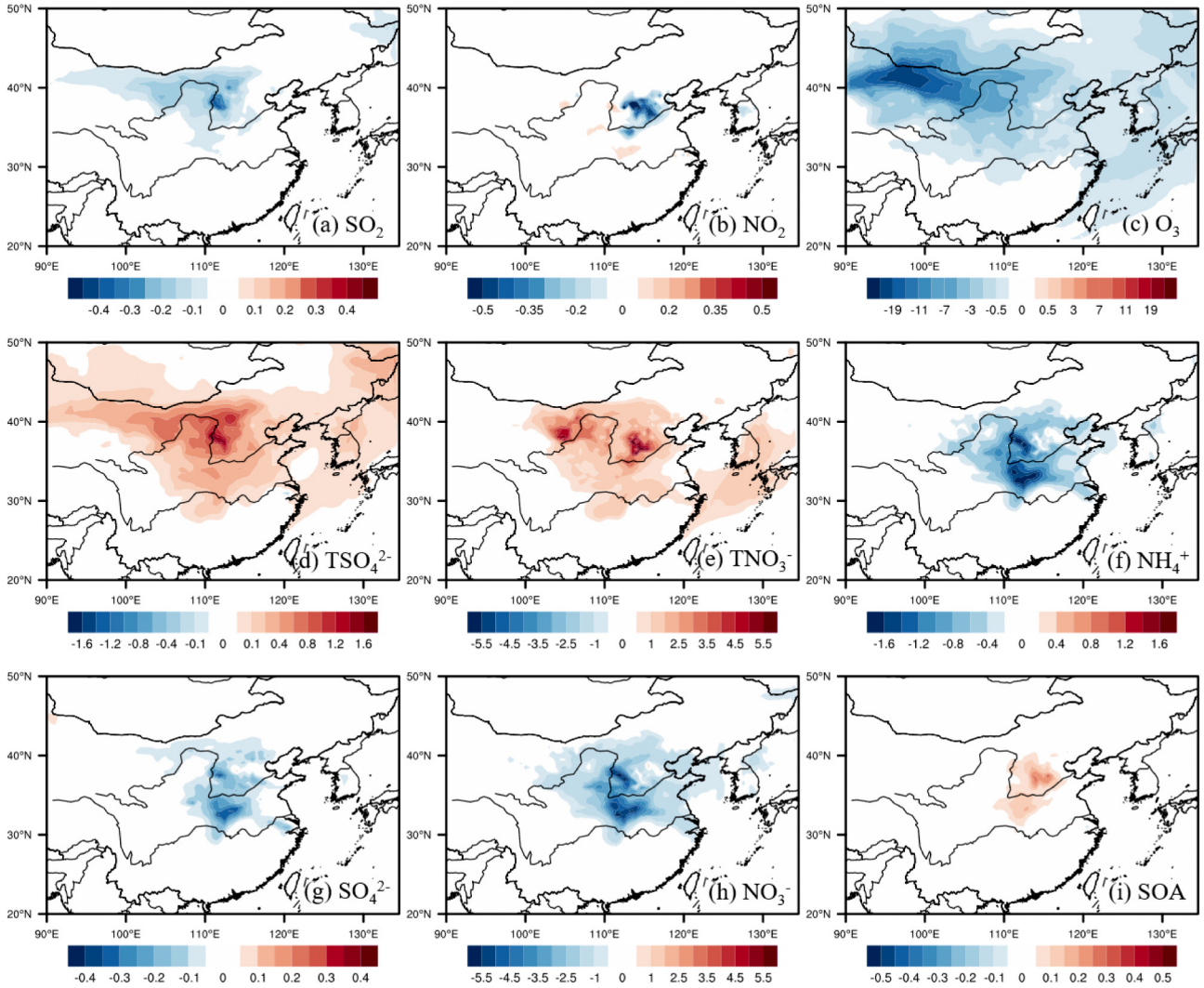

Fig. 10. The simulated mean changes in (a) SO_2, (b) NO_2, (c) O_3, (d) TSO_4^{2-}, (e) TNO_3^-, (f) NH_4^+ (g) SO_4^{2-}, (h) NO_3^-, (i) SOA concentrations due to heterogeneous reactions on dust during 14–17 March (DS1) (unit: ppb for SO_2, NO_2 and O_3, μg m^{-3} for aerosols).

Table 5 presents the domain-average changes in gas and aerosol concentrations resulting from the changes in photolysis rate and from dust heterogeneous reactions and from both processes during DS1 in the NCP and YRD regions, respectively. The changes in species concentrations by heterogeneous reactions were generally larger than those by photolysis rate change in both regions except for NO_2 and SOA. Heterogeneous reaction of NO_2 was relatively weak because of its low uptake coefficient, so NO_2 change was smaller compared with that due to photolysis rate change.

Table 5
Model simulated period and domain mean changes in gas and PM_{10} aerosol component concentrations due to heterogeneous reactions on dust surface (Het) and photolysis rate change (Pho) during DS1 (14–17, March) over the NCP and YRD, respectively (units: ppb for gas, μg m^{-3} for aerosols; Numbers in bracket are percentage change, unit: %).

		NO_2	SO_2	O_3	TSO_4^{2-}	TNO_3^-	NH_4^+	SOA
NCP	Pho	0.32	0.00	−0.89	−0.02	−0.38	−0.10	−0.40
	Het	−0.14	−0.07	−1.4	0.36	2.0	−0.46	0.06
	Pho + Het	0.15	−0.07	−2.2	0.34	1.7	−0.56	−0.28
		(1.0)	(−2.5)	(−8.4)	(13.0)	(13.5)	(−12.3)	(−4.4)
YRD	Pho	0.03	0.00	−0.18	0.00	−0.04	−0.01	−0.08
	Het	0.01	0.00	−0.39	0.05	0.61	−0.27	0.00
	Pho + Het	0.05	0.00	−0.55	0.05	0.57	−0.28	−0.08
		(0.5)	(−0.2)	(−1.9)	(3.0)	(6.8)	(−9.5)	(−1.4)

Heterogeneous reactions just indirectly affected SOA formation through perturbing OH radical in the atmosphere because there was no SOA formation through dust heterogeneous reactions, so SOA was more sensitive to OH radical change induced by the photolysis rate change. In all, the total effect of mineral dust through reducing photolysis rate and heterogeneous reactions exerted larger changes in secondary aerosols than in gas precursors, and led to changes in the domain-average sulfate, nitrate, ammonium, and SOA concentrations by 13.0 %, 13.5 %, −12.3 %, and -4.4 %, respectively, in the NCP region, which were larger than those of 3.0 %, 6.8 %, −9.5 %, and -1.4 % in the YRD region during the first dust storm episode.

4.3. Dry and wet depositions and budget of dust aerosols

Fig. 11 presents the model simulated total dust emission, dry and wet depositions, and accumulated precipitation on 14–17 March during DS1. Fig. 11a shows that dust emission mainly occurred over the Gobi Desert in southern Mongolia, with the maximum emission amount up to 90 Gg $grid^{-1}$. Dust deflation also occurred in parts of Inner Mongolia and Northeast China. Dry deposition of mineral dust occurred over wide areas from dust source regions to the western Pacific Ocean, with the maximum amount up to 27 Gg $grid^{-1}$ in eastern Mongolia and portions of western Inner Mongolia (Fig. 11b). The NCP region experienced dry deposition of ~5 Gg $grid^{-1}$, while the YRD region including Nanjing and Shanghai

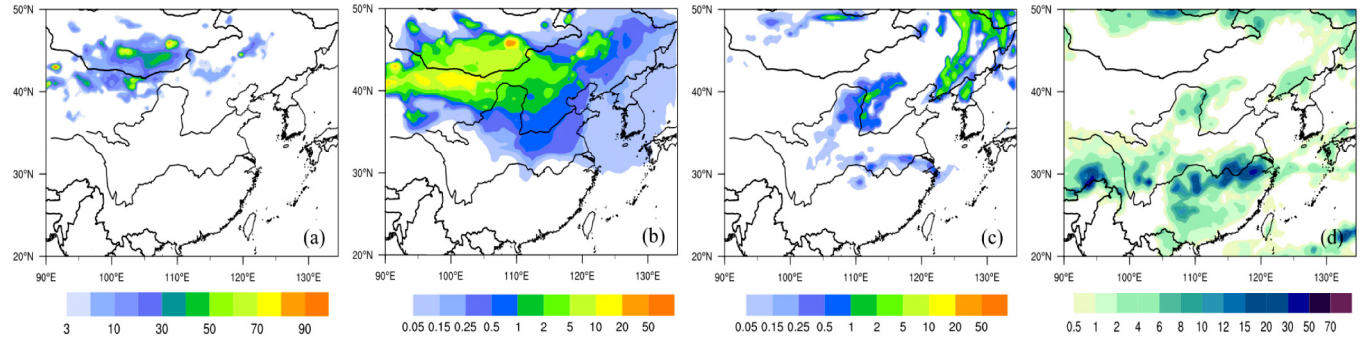

Fig. 11. The simulated (a) emission, (b) dry deposition, (c) wet deposition of dust (unit: Gg grid^{-1}) and (d) accumulated precipitation (mm) during DS1 on 14–17 March 2021.

received dry deposition of ~0.25 Gg grid^{-1}. Dry deposition amount exceeding 0.05 Gg grid^{-1} generally occurred in the YRD and the areas north of the Yangtze River of East China, reflecting the major areas affected by mineral dust. Fig. 11d shows the model simulated accumulated precipitation during 14–17 March 2021. During DS1, precipitation was scarce over the dust source regions except for the middle reaches of the Yellow River, where precipitation was 2–8 mm. Meanwhile, an apparent rain belt occurred along the Yangtze River and over portions of Northeast China, with the maximum precipitation reaching 50 mm in the lower reaches of the Yangtze River. The distribution of wet deposition generally resembled that of precipitation, but the maximum wet deposition reached 5.0 Gg grid^{-1} in the middle reaches of the Yellow River and eastern parts of Northeast China, due to the combined effect of higher dust concentration and precipitation there (Fig. 11c). Wet depositions were also high (up to 1.0 Gg grid^{-1}) in the middle and lower reaches of the Yangtze River, which was mainly due to the maximum precipitation in those regions. It is noteworthy that in the middle reaches of the Yellow River, wet deposition was comparable to dry deposition, and in most areas of Northeast China and portions of the Yangtze River, wet deposition apparently exceeded dry deposition, which demonstrated the importance of wet scavenging and wet deposition of dust aerosols to terrestrial ecosystem. However, dry deposition over the western Pacific Ocean was apparently larger than wet deposition, due to less precipitation over the Ocean during the dust storm period (Fig. 11d).

Fig. 12 presents the bin-resolved dry and wet deposition over the three land use categories (i.e., dust source regions, Area1 (shown in Fig. S1a); Mainland China other than the dust source regions, Area2; the western Pacific Ocean, Area3) during the first dust storm period of 14–17 March 2021. Fig. 12a shows dry deposition amount in each dust size bin over the three land use categories. It is noticed that dry deposition over dust source regions was apparently higher than that over downwind land and ocean areas because dust mass concentration was evidently higher over source regions. Dry deposition is determined by dust concentration and dry deposition velocity. In the dust source regions, coarse dust concentration dominated over fine dust concentration and dry deposition velocity increased with particle size, leading to a general increase of dry deposition amount with size bin, and the maximum dry deposition existed in the largest bin (the 10th bin, 27–42 μm), which accounted for approximately 26 % of the total dry deposition amount. In Area2 and Area3, which were located downwind of the deserts, coarse dust particle gradually deposited during long-range transport, leaving most airborne dust particles in fine and medium size, and because dry deposition velocity increased with particle size for the 10 bins, dry deposition tended to peak in the 7th bin (7–11 μm). Dry deposition in the 7th bin accounted for approximately 27 % and 29 % of the total dry deposition amounts over Area2 and Area3, respectively. Different from dry deposition, wet deposition in Area1 was lower than that in Area 2 (Fig. 12b), especially for larger size bin, because precipitation was much less in the deserts where large particle dominated, and the difference in wet deposition between Area1 and Area2 was small for fine particles (the first 4 bins) because fine particle could be transported farther to areas adjacent to Area2 with precipitation. It is noteworthy that wet deposition peaked in the 6th size bin (4.7–7 μm) for all the three land use categories. Wet deposition is determined by dust concentration and wet scavenging coefficient, which increases with precipitation and with particle size for the 10 bins. The size dependence of wet deposition is resulted from the combined effect of size-resolved dust concentration and precipitation (scavenging coefficient), for example, as Fig. 11d shown, precipitation was moderately high in the middle reaches of the Yellow River, where dust particle mostly settled in coarse-medium size range due to the proximity to deserts, leading to a moderate wet deposition in this size range, however, in the middle and lower reaches of the Yangtze River, where precipitation was highest, most dust particles mostly settled in medium-fine size range, which may result in a larger wet deposition in this size range over Area2. The peak wet deposition in the 6th bin accounted for approximately 33 %, 25 % and 32 % of the total wet deposition amounts over Area1 to Area3, respectively.

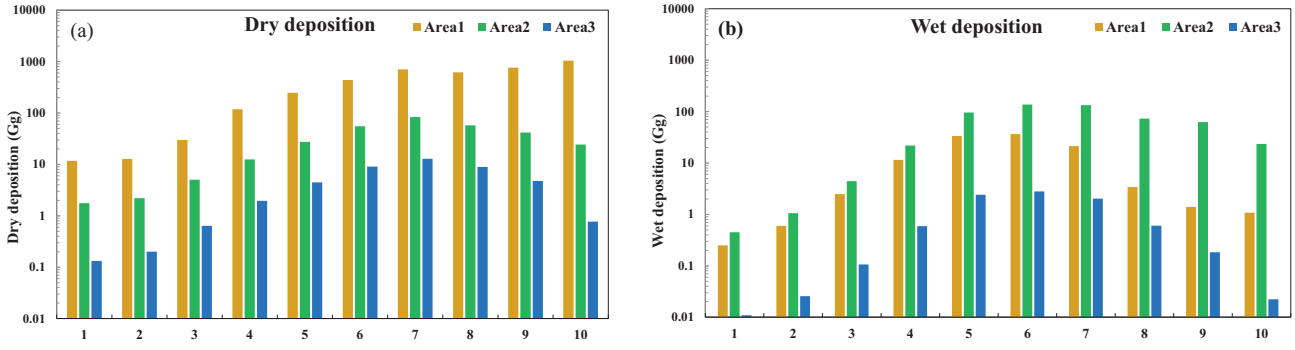

Fig. 12. The simulated bin-resolved dust (a) dry deposition, (b) wet deposition over the three land use categories during DS1 on 14–17 March 2021.

Table 6 presents the dust budget for the three categories during the two dust storm periods of 14–17 March (DS1) and 27–30 March (DS2), and during the entire study period of 10–31 March 2021. For DS1, the dust emission over the source regions was estimated to be 9.8 Tg, in which barren land and grasslands contributed 7.3 Tg and 2.5 Tg, respectively. Dry deposition over the source region was estimated to be 4.0 Tg, most of which were deposited to barren land. Dry deposition over mainland China other than the source regions was 0.31 Tg, much larger than that over the Western Pacific Ocean (0.04 Tg). Wet deposition over source regions was relatively low (0.11 Tg), but about 0.55 Tg of dust was scavenged by precipitation onto China other than the source regions, with very little wet deposition onto the oceans. It is noteworthy that wet deposition amount was remarkably larger than dry deposition over mainland China except for the dust source regions.

It is noteworthy that the dust emission in DS1 (9.8 Tg) was larger than that in DS2 (9.2 Tg), and the dry deposition amount over source regions in DS1 (4.0 Tg) was also larger than that in DS2 (3.1 Tg), however, both dry and wet depositions over mainland China other than source regions and over oceans in DS2 were larger than those in DS1, which could be associated with potentially wider spread of DS2 over downwind areas and larger precipitation during the DS2 period. For the entire study period during 10–31 March 2021, the total dust emission amount reached 31.4 Tg, in which dust emissions during DS1 and DS2 account for approximately 61 % of the total emission (19 Tg). Total dry deposition were estimated to be 13.78 Tg, in which 11.9 Tg were deposited onto dust source regions, and remaining 1.88 Tg on downwind areas including oceans. Wet depositions were totally 4.75 Tg in the study domain, in which 1.58 Tg on source regions, 2.9 and 0.27 Tg on mainland China other than source regions and oceans, respectively. In mass balance, 12.87 Tg of dust aerosols (41 % of the total dust emission) were suspended in the atmosphere and may undergo long-range transport to other regions of the world. It is noticeable that wet deposition (2.9 Tg) was about two times the dry deposition (1.5 Tg) over mainland China downwind of dust source regions, whereas over the western Pacific Ocean, wet deposition and dry deposition were comparable in magnitude. This demonstrates the important role of wet scavenging processes in dust sink and inputs to terrestrial ecosystem and oceans in the dust storm season.

In previous studies, Du et al. (2018) presented the calculated dust emission of 110 Tg yr^{-1} for dust diameter smaller than 10 μm from the Gobi and Taklimakan Deserts of China from 2001 to 2014 with an integrated wind erosion modeling system. Song et al. (2017) estimated with WRF-Chem an annual mean dust emission (diameter < 40 μm) of 67.4 Tg yr^{-1} from the Gobi and Taklimakan Deserts during 1980–2015. In this study, the dust emission (diameter < 42 μm) is estimated to be 31.4 Tg, suggesting the stronger dust emission than before considering this estimation is just for the Gobi Desert during a short time period of 10–31 March 2021. Wang et al. (2021) reported the field measurement of dust deposition amount of 19.69 g m^{-2} (approximately 0.2 Gg $grid^{-1}$ day^{-1}) in the Otindag Desert (about 600 km southeast of the Gobi Desert) from August 2018 to July 2019, which is lower than the estimation of about 0.8 Gg $grid^{-1}$ day^{-1} in the same region (shown in Fig. 11b) in this study, this is expected because the dust storm in March 2021 is much stronger than that in 2019.

Table 6
Dust Budget for typical land use categories during DS1 of 14–17 March, DS2 of 27–30 March and during the entire study period of 10–31 March, 2021 (unit: Tg).

DS1	Emission	Dry deposition	Wet deposition
Source region (Barren)	7.3	2.8	0
Source region (Grassland)	2.5	1.2	0.11
China other than source region	0	0.31	0.55
Ocean or sea	0	0.04	0.01
DS2			
Source region (Barren)	6.6	1.7	0.17
Source region (Grassland)	2.6	1.4	0.36
China other than source region	0	0.4	0.90
Ocean or sea	0	0.12	0.05
10–31 March			
Source region (Barren)	25.0	8.2	0.38
Source region (Grassland)	6.4	3.7	1.2
China other than source region	0	1.5	2.9
Ocean or sea	0	0.38	0.27

To help understand global dust distribution and cycling, it is meaningful to compare the dust budget in East Asia from this study with those in other deserts of the world in previous studies. Laurent et al. (2010) simulated Saharan dust emission, transport, and deposition from 10 May to 5 June 2006 by using a regional model COSMO-MUSCAT, and estimated 78 Tg dust emission during the studied period, in which about 67 % was deposited in the vicinity of source areas over North Africa and close marine areas, and 33 % was transported toward other continents and remote ocean areas. Anisimov et al. (2018) investigated strong mesoscale haboob dust storms in April 2007 in the central Arabian Peninsula by using WRF-Chem, and estimated approximately 25.5 Tg of dust emission from the Arabian Peninsula during the 10-day period on 5–14 April, in which 17.9 Tg (70 %) was deposited to the ground and 30 % of the total dust particles was transported outside the study area. The dust emissions (31.4 Tg) generated from the Gobi Desert in East Asia during the 22-day study period from this study appear to be comparable to those in the Middle East deserts and smaller than those in the Saharan deserts, and a larger fraction of total dust particles (41 %) generated in the Gobi Desert are transported out of East Asia to other continents than that (approximately 30 %) in the Middle East and Saharan deserts.

5. Conclusions

Dust storms during 10–31 March 2021 over East Asia were synthetically investigated by the RAQMS model coupled with a developed dust model by using up-to-date land use data and soil texture map and by introducing soil moisture in calculation of threshold friction velocity. The model results are validated against a variety of ground, vertical and satellite observations for meteorological variables, soil liquid water content, PM_{10} and $PM_{2.5}$ chemical components, AOD, vertical profile of extinction coefficient, as well as surface shortwave radiation, which demonstrate an overall good ability of the model system in reproducing the spatial-temporal distribution of dust storms, aerosol concentrations and properties.

The first dust storm was originated from the Gobi Desert in southern Mongolia on 14 March, with the dust emission flux reaching 2785 μg m^{-2} s^{-1} and the maximum dust concentration exceeding 18,000 μg m^{-3} in the dust deflation region. The dust storm arrived at the NCP in the morning of 15 March, leading to the maximum hourly PM_{10} observations up to 7506 μg m^{-3}, 1887 μg m^{-3}, and 2704 μg m^{-3} in Beijing, Tianjin, and Shijiazhuang, respectively. On 27 March, the second dust storm broke out in the deserts of eastern Mongolia, with the maximum dust emission flux reaching 1200 μg m^{-2} s^{-1}.

Surface shortwave radiation was consistently reduced over broad areas of North China during the first dust storm episode of 14–17 March. Beijing experienced the maximum decrease in hourly surface shortwave radiation by up to 313.4 W m^{-2} (72 %) at 10:00 LST on 15 March, demonstrating the significant radiative impact of the dust storm. The extinction of solar radiation by the dust storm led to a consistent reduction in the photolysis rates of NO_2 and O_3 from the Gobi Desert to downwind East China and consequently the decreases in O_3 and secondary aerosols. Total sulfate and nitrate concentrations consistently increased over the middle reaches of the Yellow River and the NCP region, mainly due to the increases in sulfate and nitrate produced through heterogeneous reactions on dust surface, whereas sulfate, nitrate and ammonium in the atmosphere were decreased correspondingly.

Sulfate and nitrate formation through heterogeneous reactions were enhanced in the dust backflow on 16–17 March by approximately 18 % and 24 % on average in the NCP, due to increasing precursor concentrations, moderate wind speed with increasing relative humidity. The changes in chemical species by heterogeneous reactions were larger than those due to the photolysis rate change. Heterogeneous reactions and photolysis

rate reduction by mineral dust jointly led to average changes in sulfate, nitrate, ammonium, and SOA by 13.0 %, 13.5 %, −12.3 %, and -4.4 %, respectively, in the NCP region during DS1, larger than the changes in the YRD region.

The maximum dry deposition existed in the 27–42 μm size range in dust source regions, whereas it settled in 7–11 μm in downwind land and ocean areas. Wet deposition peaked in the 4.7–7 μm size range. During DS1, dust emission over the source regions was totally 9.8 Tg, while dry and wet depositions were estimated to be 4.35 Tg and 0.67 Tg in the study domain. Wet deposition amount was remarkably larger than dry deposition over mainland China except the dust source regions. Dust emission and dry deposition in DS1 were larger than that in DS2 in source regions, but dry and wet depositions over mainland China other than dust source regions and over oceans in DS2 were larger than those in DS1. For 10–31 March 2021, the total dust emission, dry and wet depositions were estimated to be 31.4 Tg, 13.78 Tg and 4.75 Tg, with remaining 12.87 Tg of dust aerosols (41 % of the total dust emission) suspending in the atmosphere or being transported out of East Asia. More dust particles (41 % of dust emission) generated from the Asian Gobi Desert can be transported to other continents than those (approximately 30 %) from the Middle East and Saharan deserts.

While this study reveals the significant environmental impacts of the severe dust storm over East Asia, there could be potential uncertainties in model simulations which may be further addressed: 1.) given the biases in vertical gradients of wind and relative humidity, PBL scheme needs to be improved to better represent vertical diffusivity. 2.) Precipitation is generally underpredicted by WRF over China, which could underestimate wet deposition and overestimate airborne dust aerosols. 3.) Size distribution of dust emission needs to be represented more realistically with dust model development and constraints from up-to-date field measurements. 4.) uptake coefficients on dust surface may vary largely for various types of mineral dust in different environmental conditions, which require data from laboratory experiments and field measurements to reduce the uncertainty range. In addition, the effects of dust aerosols on cloud and precipitation as cloud condensation nuclei or ice nuclei and on climate at regional and global scales will be explored in the future.

CRediT authorship contribution statement

Lin Liang: Investigation, Formal analysis, Software, Validation, Writing – original draft

Zhiwei Han: Methodology, Investigation, Writing – review & editing, Supervision

Jiawei Li: Software, Validation, Investigation

Xiangao Xia: Data curation, Resources, Validation

Yele Sun: Data curation, Resources

Hong Liao: Data curation, Analysis

Ruiting Liu: Data curation, Validation

Mingjie Liang: Data curation, Analysis

Yuan Gao: Data curation, Resources

Renjian Zhang: Resources, Analysis

Data availability

Dust model code is available upon request to the corresponding author (hzw@mail.iap.ac.cn).

Data availability

Data will be made available on request.

Declaration of competing interest

The authors declare that they have no known competing financial interests or personal relationships that could have appeared to influence the work reported in this paper.

Acknowledgments

This study was supported by the National Key R&D Program of China (2019YFA0606802), the National Natural Science Foundation of China (92044302) and the Jiangsu Collaborative Innovation Center for Climate Change.

Appendix A. Supplementary data

Supplementary data to this article can be found online at https://doi.org/10.1016/j.scitotenv.2022.158459.

References

An, J.L., Ueda, H., Wang, Z., Matsuda, K., Kajino, M., Cheng, X., 2002. Simulations of monthly mean nitrate concentrations in precipitation over East Asia. Atmos. Environ. 36, 4159–4171.

Anisimov, A., Axisa, D., Kucera, P.A., Mostamandi, S., Stenchikov, G., 2018. Observations and cloud-resolving modeling of haboob dust storms over the Arabian peninsula. J. Geophys. Res. Atmos. 123, 147–179.

Carmichael, G.R., 2008. Model intercomparison study for Asia. Phase II. Atmos. Environ. 42, 3465–3467.

Chang, J.S., Brost, R.A., Isaksen, I.S.A., Madronich, S., Middleton, P., Stockwell, W.R., Walcek, C.J., 1987. A three-dimensional Eulerian acid deposition model: physical concepts and formulation. J. Geophys. Res. Atmos. 92, 14681–14700.

Chen, F., Dudhia, J., 2001. Coupling an advanced land surface–hydrology model with the Penn State-NCAR MM5 modeling system. Part I: model implementation and sensitivity. Mon. Wea. Rev. 129 (4), 569–585.

Chen, L., Gao, Y., Zhang, M., Fu, J.S., Zhu, J., Liao, H., Li, J., Huang, K., Ge, B., Wang, X., Lam, Y.F., Lin, C.Y., Itahashi, S., Nagashima, T., Kajino, M., Yamaji, K., Wang, Z., Kurokawa, J., 2019. MICS-Asia III: multi-model comparison and evaluation of aerosol over East Asia. Atmos. Chem. Phys. 19, 11911–11937.

DeMott, P.J., Prenni, A.J., Liu, X., Kreidenweis, S.M., Petters, M.D., Twohy, C.H., Richardson, M.S., Eidhammer, T., Rodgers, D.C., 2010. Predicting global atmospheric ice nuclei distributions and their impacts on climate. Proc. Natl. Acad. Sci. U. S. A. 107 (25), 11217–11222.

Dentener, F.J., Carmichael, G.R., Zhang, Y., Lelieveld, J., Crutzen, P.J., 1996. Role of mineral aerosol as a reactive surface in the global troposphere. J. Geophys. Res. 101, 22869–22889.

Donahue, N.M., Robinson, A.L., Stanier, C.O., Pandis, S.N., 2006. Coupled partitioning, dilution, and chemical aging of semivolatile organics. Environ. Sci. Technol. 40, 2635–2643.

Dong, X.Y., Fu, J.S., Huang, K., Tong, D., Zhuang, G.S., 2016. Model development of dust emission and heterogeneous chemistry within the community multiscale air quality modeling system and its application over East Asia. Atmos. Chem. Phys. 16, 8157–8180. https://doi.org/10.5194/acp-16-8157-2016.

Du, H., Wang, T., Xue, X., Li, S., 2018. Modelling of sand/dust emission in northern China from 2001 to 2014. Geoderma 330, 162–176.

Faridi, S., Rahmani, S., Hashemi, N., Ghobadian, S., Zokaei, M.S., 2021. The economic effects of dust storm. J. Health 11 (5), 699–713.

Filonchyk, M., 2022. Characteristics of the severe march 2021 Gobi Desert dust storm and its impact on air pollution in China. Chemosphere 287 (1), 132219. https://doi.org/10.1016/j.chemosphere.2021.132219.

Gery, M.W., Whitten, G.Z., Killus, J.P., Dodge, M.C., 1989. A photochemical kinetics mechanism for urban and regional scale computer modeling. J. Geophys. Res. 94, 12925–12956.

Ghan, S., Zaveri, R.A., 2007. Parameterization of optical properties for hydrated internally mixed aerosol. J. Geophys. Res. 112, D10201. https://doi.org/10.1029/2006JD007927.

Ginoux, P., Chin, M., Tegen, I., Prospero, J.M., Holben, B., Dubovik, O., Lin, S.J., 2001. Sources and distributions of dust aerosols simulated with the GOCART model. J. Geophys. Res. 106, 20255–20273. https://doi.org/10.1029/2000JD000053.

Ginoux, P., Prospero, J.M., Torres, O., Chin, M., 2004. Long-term simulation of global dust distibution with the GOCART model: correlation with North Atlantic oscillation. Environ. Model Softw. 19, 113–128.

Han, Z.W., 2007. A regional air quality model: evaluation and simulation of O3 and relevant gaseous species in East Asia during spring 2001. Environ. Model Softw. 22, 1328–1336.

Han, Z.W., Ueda, H., Matsuda, K., Zhang, R.J., Arao, K., Kanai, Y., Hasome, H., 2004. Model study on particle size segregation and deposition during Asian dust events in march 2002. J. Geophys. Res. 109, D19205. https://doi.org/10.1029/2004JD004920.

Han, Z.W., Ueda, H., Sakurai, T., 2006. Model study on acidifying wet deposition in East Asia during wintertime. Atmos. Environ. 40, 2360–2373.

Han, Z.W., Sakurai, T., Ueda, H., Carmichael, G.R., Streets, D., Hayami, H., Wang, Z., Holloway, T., Engardt, M., Hozumi, Y., Park, S.U., Kajino, M., Sartelet, K., Fung, C., Bennet, C., Thongboonchoo, N., Tang, Y., Chang, A., Matsuda, K., Amann, M., 2008a. MICS-Asia II: model intercomparison and evaluation of ozone and relevant species. Atmos. Environ. 42, 3491–3509.

Han, Z.W., Zhang, R., Wang, Q., Wang, W., Cao, J., Xu, J., 2008b. Regional modeling of organic aerosols over China in summertime. J. Geophys. Res. Atmos. 113, D11202. https://doi.org/10.1029/2007JD009436.

Han, Z.W., Li, J.W., Xia, X.A., Zhang, R.J., 2012. Investigation of direct radiative effects of aerosols in dust storm season over East Asia with an online coupled regional climate-chemistry-aerosol model. Atmos. Environ. 54, 688–699.

Han, Z.W., Xie, Z.X., Wang, G.H., Zhang, R.J., Tao, J., 2016. Modeling organic aerosols over East China using a volatility basis-set approach with aging mechanism in a regional air quality model. Atmos. Environ. 124, 186–198.
Hess, M., Koepke, P., Schuit, I., 1998. Optical properties of aerosols and clouds: the software package OPAC. Bull. Am. Meteorol. Soc. 79, 831–844.
Hong, S.Y., Lim, J.O.J., 2006. The WRF single-moment 6-class microphysics scheme (WSM6). Asia-Pac. J. Atmos. Sci. 42 (2), 129–151.
Hong, S.Y., Noh, Y., Dudhia, J., 2005. A new vertical diffusion package with an explicit treatment of entrainment processes. Mon. Weather Rev. 134, 2318–2341.
Iacono, M.J., Delamere, J.S., Mlawer, E.J., Shephard, M.W., Clough, S.A., Collins, W.D., 2008. Radiative forcing by long-lived greenhouse gases: calculations with the AER radiative transfer models. J. Geophys. Res. 113, D13103. https://doi.org/10.1029/2008JD009944.
Jacob, D.J., 2000. Heterogeneous chemistry and tropospheric ozone. Atmos. Environ. 34, 2131–2159.
Jin, J., Pang, M., Segers, A., Han, W., Fang, L., Li, B., Feng, H., Lin, H.X., Liao, H., 2022. Inverse modeling of the 2021 spring super dust storms in East Asia. Atmos. Chem. Phys. 22 (6393–6410), 2022. https://doi.org/10.5194/acp-22-6393-2022.
Kaufman, Y.J., Tanre, D., Boucher, O., 2002. A satellite view of aerosols in the climate system. Nature 419, 215–223.
Laurent, B., Tegen, I., Heinold, B., Schepanski, K., Weinzierl, B., 2010. A model study of saharan dust emissions and distributions during the samum-1 campaign. J. Geophys. Res. 115, D21210. https://doi.org/10.1029/2009JD012995.
Li, J.W., Han, Z.W., 2010. A modeling study of the impact of heterogeneous reactions on mineral aerosol surfaces on tropospheric chemistry over East Asia. Particuology 8, 433–441.
Li, J.W., Han, Z.W., 2015. Investigation of three-dimensional evolution of east Asian dust storm by modeling and remote sensing measurements. Adv. Meteorol. 483476. https://doi.org/10.1155/2015/483476.
Li, J.W., Han, Z.W., 2016. A modeling study of severe winter haze events in Beijing and its neighboring regions. Atmos. Res. 170, 87–97.
Li, N., Gu, W., Xie, F., Du, Z., 2004. Threshold value response of soil moisture to dust storm: a case study of mid western Inner Mongolia Autonomous Region. J. Nat. Dis. Sci. 13, 44–49.
Li, J.W., Han, Z.W., Zhang, R.J., 2011. Model study of atmospheric particulates during dust storm period in march 2010 over East Asia. Atmos. Environ. 45, 3954–3964.
Li, M.M., Wang, T.J., Han, Y., Xie, M., Li, S., Zhuang, B.L., Chen, P.L., 2017. Modeling of a severe dust event and its impacts on ozone photochemistry over the downstream Nanjing megacity of eastern China. Atmos. Environ. 160, 107–123.
Li, J.W., Han, Z.W., Yao, X., 2018. A modeling study of the influence of sea salt on inorganic aerosol concentration, size distribution, and deposition in the western Pacific Ocean. Atmos. Environ. 188, 157–173.
Li, J., Han, Z.W., Li, J.W., Liu, R.T., Wu, T.F., Liang, L., Zhang, R.J., 2020. The formation and evolution of secondary organic aerosol during haze events in Beijing in wintertime. Sci. Total Environ. 703, 134937. https://doi.org/10.1016/j.scitotenv.2019.134937.
Li, J., Han, Z.W., Sun, Y.L., Liu, R.T., Li, J.W., Liang, L., 2021. The chemical formation pathways of secondary organic aerosols in the Beijing-Tianjin-Hebei region in wintertime. Atmos. Environ. 244, 117996. https://doi.org/10.1016/j.atmosenv.2020.117996.
Liang, P., Chen, B., Yang, X.P., Liu, A.R., Mackenzie, L., Zhang, D.G., 2022. Revealing the dust transport processes of the 2021 mega dust storm event in northern China. Sci. Bull. 67 (1), 21–24.
Liu, S., Xing, J., Sahu, S.K., Liu, X.L., Liu, S.C., Jiang, Y.Q., Zhang, H.L., Li, S.W., Ding, D., Chang, X., Wang, S.X., 2021. Wind-blown dust and its impacts on particulate matter pollution in northern China: current and future scenarios. Environ. Res. Lett. 16, 114041. https://doi.org/10.1088/1748-9326/ac31ec.
Louis, J.F., 1979. A parametric model of vertical eddy fluxes in the atmosphere. Bound.-Layer Meteorol. 17, 187–202.
Louvaris, E.E., Florou, K., Karnezi, E., Papanastasiou, D.K., Gkatzelis, G.I., Pandis, S.N., 2017. Volatility of source apportioned wintertime organic aerosol in the city of Athens. Atmos. Environ. 158, 138–147.
Ma, S., Zhang, X., Gao, C., Tong, D.Q., Xiu, A., Wu, G., Cao, X., Huang, L., Zhao, H., Zhang, S., Ibarra-Espinosa, S., Wang, X., Li, X., Dan, M., 2019. Multimodel simulations of a spring time dust storm over northeastern China: implications of an evaluation of four commonly used air quality models (CMAQv5.2.1, CAMxv6.50, CHIMERE v2017r4, and WRF-Chemv3.9.1). Geosci. Model Dev. 12, 4603–4625.
Madronich, S., Flocke, S., 1999. The role of solar radiation in atmospheric chemistry. Environ. Photochem. 1–26.
Marticorena, B., Bergametti, G., 1995. Modeling the atmospheric dust cycle: 1. Design of a soil-derived dust emission scheme. J. Geophys. Res. 100, 16415–16430.
Meng, Z., Dabdub, D., Seinfeld, J.H., 1998. Size-resolved and chemically resolved model of atmospheric aerosol dynamics. J. Geophys. Res. 103, 3419–3435.
Nenes, A., Pandis, S.N., Pilinis, C., 1998. ISORROPIA: a new thermodynamic equilibrium model for multiphase multicomponent inorganic aerosols. Aquat. Geochem. 4, 123–152.
Pan, X.L., Uno, I., Wang, Z., Nishizawa, T., Sugimoto, N., Yamamoto, S., Kobayashi, H., Sun, Y.L., Fu, P.Q., Tang, X., Wang, Z.F., 2017. Real time observational evidence of changing asian dust morphology with the mixing of heavy anthropogenic pollution. Sci. Rep. 7, 335. https://doi.org/10.1038/s41598-017-00444-w.
Petters, M.D., Kreidenweis, S.M., 2007. A single parameter representation of hygroscopic growth and cloud condensation nucleus activity. Atmos. Chem. Phys. 7, 1961–1971.
Pye, H.O.T., Seinfeld, J.H., 2010. A global perspective on aerosol from low-volatility organic compounds. Atmos. Chem. Phys. 10, 4377–4401.
Seinfeld, J.H., Carmichael, G., Arimoto, R., Conant, W.C., Brechtel, F.J., Bates, T.S., Cahill, T.A., Clarke, A.D., Doherty, S.J., Flatau, F.J., Huebert, B.J., Kim, J., Markowicz, K.M., Quinn, P.K., Russell, L.M., Russell, P.B., Shimizu, A., Song, C.H., TanShag, Y., Uno, I., Vogelmann, A.M., Weber, R.J., Woo, J., Zhang, X.Y., 2004. ACE-ASIA: regional climatic and atmospheric chemical effects of Asian dust and pollution. Bull. Am. Meteorol. Soc. 85, 367–380.
Shao, Y.P., 2001. A model for mineral dust emission. J. Geophys. Res. Atmos. 106, 20239–20254.
Shao, Y.P., Dong, C.H., 2006. A review on east Asian dust storm climate, modeling and monitoring. Glob. Planet. Change 52, 1–22.
Song, H., Wang, K., Zhang, Y., Hong, C., Zhou, S., 2017. Simulation and evaluation of dust emissions with WRF-chem (v3.7.1) and its relationship to the changing climate over East Asia from 1980 to 2015. Atmos. Environ. 167, 511–522.
Tang, M.J., Huang, X., Lu, K., Ge, M.F., Li, Y.J., Cheng, P., Zhu, T., Ding, A.J., Zhang, Y.H., Gligorovski, S., Song, W., Ding, X., Bi, X.H., Wang, X.M., 2017. Heterogeneous reactions of mineral dust aerosol: implications for tropospheric oxidation capacity. Atmos. Chem. Phys. 17, 11727–11777.
Tian, R., Ma, X., Zhao, J.Q., 2021a. A revised mineral dust emission scheme in GEOS-chem: improvements in dust simulations over China. Atmos. Chem. Phys. 21, 4319–4337.
Tian, R., Ma, X., Sha, T., Pan, X., Wang, Z., 2021b. Exploring dust heterogeneous chemistry over China: insights from field observation and GEOS-chem simulation. Sci. Total Environ. 798, 149307. https://doi.org/10.1016/j.scitotenv.2021.149307.
Uno, I., Amano, H., Emori, S., Kinoshita, K., Matsui, I., Sugimoto, N., 2001. Transpacific yellow sand transport observed in April 1998. J. Geophys. Res. 106, 18331–18344.
Wagner, C., Schuster, G., Crowley, J.N., 2009. An aerosol flow tube study of the interaction of N2O5 with calcite, Arizona dust and quartz. Atmos. Environ. 43, 5001–5008.
Wang, H., Shi, G.Y., Teruo, A., Wang, B., Zhao, T.L., 2004. Radiative forcing due to dust aerosol over East Asia-North Pacific region during spring 2001. Chin. Sci. Bull. 49, 2212–2219.
Wang, X., Cai, D., Li, D., Lou, J., Zheng, Y., Hu, S., Liu, F., 2021. Dust deposition and its significance to soil nutrients in the Otindag DesertChina. J. Arid Environ. 194, 104612.
van der Werf, G.R., Randerson, J.T., Giglio, L., van Leeuwen, T.T., Chen, Y., Rogers, B.M., Mu, M., van Marle, M.J.E., Morton, D.C., Collatz, G.J., Yokelson, R.J., Kasibhatla, P.S., 2017. Global fire emissions estimates during 1997–2016. Earth Syst. Sci. Data 9, 697–720.
Yin, Z.C., Wan, Y., Zhang, Y.J., Wang, H.J., 2022. Why super sandstorm 2021 in North China. Natl. Sci. Rev. 9 (03), 119–127.
Zhang, X.Y., Gong, S.L., Shen, Z.X., Mei, F.M., Xi, X.X., Liu, L.C., Zhou, Z.J., Wang, D., Wang, Y.Q., Cheng, Y., 2003. Characterization of soil dust aerosol in China and its transport and distribution during 2001 ACE-ASIA: network observations. J. Geophys. Res. 108 (D9), 4261. https://doi.org/10.1029/2002JD002632.
Zhang, C.X., Wang, Y.Q., Hamilton, K., 2011. Improved representation of boundary layer clouds over the Southeast Pacific in ARW-WRF using a modified Tiedtke cumulus parameterization scheme. Mon. Wea. Rev. 139 (11), 3489–3513.
Zhang, X.X., Sharratt, B., Liu, L.Y., Wang, Z.F., Pan, X.L., Lei, J.Q., Wu, S.X., Huang, S.Y., Guo, Y.H., Li, J., Tang, X., Yang, T., Tian, Y., Chen, X.S., Hao, J.Q., Zheng, H.T., Yang, Y.Y., Lyu, Y.L., 2018. East asian dust storm in may 2017: observations, modelling, and its influence on the Asia-Pacific region. Atmos. Chem. Phys. 18, 8353–8371.
Zhang, L., Zhang, H.S., Li, Q.H., Cai, X.H., Song, Y., 2022. Vertical dispersion mechanism of long-range transported dust in Beijing: effects of atmospheric turbulence. Atmos. Res. 269, 0169–8059.
Zhao, T.L., Gong, S.L., Zhang, X.Y., Jaffe, D.A., 2008. Asian dust storm influence on north american ambient PM levels: observational evidence and controlling factors. Atmos. Chem. Phys. 8, 2717–2728.
Zheng, B., Zhang, Q., Geng, G.B., Chen, C.H., Shi, Q.R., Cui, M.S., Lei, Y., He, K.B., 2021. Changes in China's anthropogenic emissions and air quality during the COVID-19 pandemic in 2020. Earth Syst. Sci. Data 13, 2895–2907.